

1            Highly time-resolved urban aerosol characteristics during  
2            springtime in Yangtze River Delta, China: Insights from soot  
3                            particle aerosol mass spectrometry

4  
5            Junfeng Wang,<sup>1,2</sup> Xinlei Ge,<sup>1,\*</sup> Yanfang Chen,<sup>1</sup> Yafei Shen,<sup>1</sup> Qi Zhang,<sup>1,3</sup> Yele Sun,<sup>4</sup>  
6                            Jianzhong Xu,<sup>5</sup> Shun, Ge,<sup>6</sup> Huan Yu,<sup>1</sup> Mindong Chen<sup>1,\*</sup>

7  
8            <sup>1</sup>Jiangsu Key Laboratory of Atmospheric Environment Monitoring and Pollution  
9            Control (AEMPC), Collaborative Innovation Center of Atmospheric Environment and  
10            Equipment Technology (CIC-AEET), School of Environmental Science and  
11            Engineering, Nanjing University of Information Science & Technology, Nanjing  
12            210044, China

13            <sup>2</sup>Yangzhou Environmental Monitoring Center, Yangzhou 225007, China

14            <sup>3</sup>Department of Environmental Toxicology, University of California at Davis, Davis,  
15            California 95616, United States

16            <sup>4</sup>State Key Laboratory of Atmospheric Boundary Layer Physics and Atmospheric  
17            Chemistry, Institute of Atmospheric Physics, Chinese Academy of Sciences, Beijing  
18            100029, China

19            <sup>5</sup>State Key Laboratory of Cryospheric Sciences, Cold and Arid Regions,  
20            Environmental and Engineering Research Institute, Chinese Academy of Sciences,  
21            Lanzhou 730000, China

22            <sup>6</sup>Nanjing Tianbo Environmental Technology Co., Ltd, Nanjing 210047, China

23  
24            \*Corresponding author, Email: [caxinra@163.com](mailto:caxinra@163.com); [chenmdnuist@163.com](mailto:chenmdnuist@163.com)

25                            Phone: +86-25-58731394

26  
27                            For *Atmos. Chem. Phys.*

29 **Abstract:** In this work, the Aerodyne soot particle – aerosol mass spectrometer  
30 (SP-AMS) was deployed for the first time during the spring of 2015 in urban Nanjing,  
31 a megacity in the Yangtze River Delta (YRD) of China, for online characterization of  
32 the submicron aerosols (PM<sub>1</sub>). The SP-AMS enables real-time and fast quantification  
33 of refractory black carbon (*r*BC) simultaneously with other non-refractory species  
34 (ammonium, sulfate, nitrate, chloride and organics). The average PM<sub>1</sub> concentration  
35 was found to be 28.2 μg m<sup>-3</sup>, with organics (45%) as the most abundant component,  
36 following by sulfate (19.3%), nitrate (13.6%), ammonium (11.1%), *r*BC (9.7%) and  
37 chloride (1.3%). These PM<sub>1</sub> species together can reconstruct ~44% of the light  
38 extinction during this campaign based on the IMPROVE method.  
39 Chemically-resolved mass-based size distributions revealed that small particles  
40 especially ultrafine ones (<100 nm vacuum aerodynamic diameter) were dominated  
41 by organics and *r*BC, while large particles had significant contributions from  
42 secondary inorganic species. Source apportionment of organic aerosols (OA) yielded  
43 four OA subcomponents, including hydrocarbon-like OA (HOA), cooking-related OA  
44 (COA), semi-volatile oxygenated OA (SV-OOA), and low-volatility oxygenated OA  
45 (LV-OOA). Overall, secondary organic aerosol (SOA, equal to the sum of SV-OOA  
46 and LV-OOA) dominated the total OA mass (55.5%), but primary organic aerosol  
47 (POA, equal to the sum of HOA and COA) can outweigh SOA in early morning and  
48 evening due to enhanced human activities. High OA concentrations were often  
49 associated with high mass fractions of POA and *r*BC, indicating the important role of  
50 anthropogenic emissions during heavy pollution events. The diurnal cycles of nitrate,  
51 chloride and SV-OOA both showed good anti-correlations with air temperatures,  
52 suggesting their variations were likely driven by thermodynamic equilibria and  
53 gas-to-particle partitioning. On the other hand, in contrast to other species, sulfate and  
54 LV-OOA concentrations increased during afternoon, and showed no positive  
55 correlations with relative humidity (RH), likely indicating the contribution from  
56 photochemical oxidation is dominant over that of aqueous-phase processing for their  
57 formations. The bivariate polar plots show that the SV-OOA was formed locally, and

58 the variations of hydrogen-to-carbon (H/C) and oxygen-to-carbon (O/C) ratios in the  
59 Van Krevelen space further suggests an evolution pathway of SV-OOA to LV-OOA.  
60 Our findings regarding springtime aerosol chemistry in Nanjing may have important  
61 implications for the air quality remediation in the densely populated regions.

62

## 63 **1. Introduction**

64 In recent years, high concentrations of fine particulate matter (PM<sub>2.5</sub>) have been  
65 frequently observed (Hu et al., 2015), in accompanying with the visibility impairment  
66 and occurrence of haze events across large parts of China. PM<sub>2.5</sub> also affects human  
67 health (e.g., Pope and Dockery, 2006;Cao et al., 2012), regional and global climate  
68 directly by absorbing and scattering solar radiation or indirectly by acting as cloud  
69 condensation nuclei and ice nuclei (e.g.,Ghan and Schwartz, 2007;Pöschl, 2005), and  
70 the earth's ecosystem (Carslaw et al., 2010). These effects are predominantly  
71 dependent upon the physical and chemical characteristics of fine particles, such as  
72 mass concentration, chemical composition, size distribution, and hygroscopicity, all of  
73 which are influenced by the emission sources and transformation and evolution  
74 processes in the atmosphere.

75 The Yangtze River Delta (YRD) region is one of the most populated and  
76 economically developed areas in China, but it is also facing with severe air pollution  
77 lately. Nanjing, as one of the major megacities in this region, has a daily PM<sub>2.5</sub> mass  
78 concentration varying between 33-234  $\mu\text{g m}^{-3}$  during November 2011 - August 2012,  
79 with an mean value of 106  $\mu\text{g m}^{-3}$ , which is 4.2 times the WHO air quality standard of  
80 25  $\mu\text{g m}^{-3}$  (Shen et al., 2014). PM<sub>2.5</sub> pollution is significantly elevated during hazy  
81 days, for example, a daily average of 282  $\mu\text{g m}^{-3}$  was observed for a heavily polluted  
82 day (Fu et al., 2008). A number of studies regarding aerosol chemistry in Nanjing  
83 have been conducted, and identified various inorganic components (sulfate, nitrate,  
84 ammonium and heavy metals, etc.) (e.g., Wang et al., 2003;Hu et al., 2012;Qi et al.,  
85 2016) and hundreds of organic species (carboxylic/dicarboxylic acids, amines and  
86 amino acids, polycyclic aromatic hydrocarbons, etc.) (Wang et al., 2011;Wang et al.,

87 2002;Yang et al., 2005;Wang et al., 2009) that contribute to the aerosol mass.  
88 However, past studies mostly employed filter-based sampling technique, which due to  
89 low time resolution (a few hours to days), is often incapable of capturing details of the  
90 atmospheric evolution processes during the typical lifecycle of aerosols (Wexler and  
91 Johnston, 2008). Subsequent offline analyses may also introduce artifacts as some  
92 semi-volatile species can evaporate during sampling and storage (Dong et al., 2012).

93 On the other hand, in the past 15 years, the Aerodyne Aerosol Mass spectrometer  
94 (AMS) (Canagaratna et al., 2007) has been widely used, and was proven to be  
95 powerful for real-time online measurements of size-resolved chemical compositions  
96 of submicron aerosols ( $PM_{10}$ ) with very fine time resolution (seconds to minutes)  
97 (Zhang et al., 2007a;Jimenez et al., 2009). The development of Aerodyne AMS began  
98 with the invention of quadruple AMS (Q-AMS) (Jayne et al., 2000), following by the  
99 compact time-of-flight AMS (C-ToF-AMS) (Drewnick et al., 2005), high resolution  
100 time-of-flight AMS (HR-ToF-AMS) (DeCarlo et al., 2006) and the soot particle AMS  
101 (SP-AMS) (Onasch et al., 2012). There are also an aerosol chemical speciation  
102 monitor (ACSM) (Ng et al., 2011) and its updated version of ToF-ACSM (Fröhlich et  
103 al., 2013), which are in particular designed for long-term unattended aerosol  
104 measurements. SP-AMS is the most advanced version, which in principle incorporates  
105 the single particle soot photometer (SP2) into the HR-ToF-AMS, and upgraded with a  
106 laser vaporizer for detecting refractory black carbon (*r*BC) and associated/coated  
107 species that cannot be measured by other types of AMS.

108 Recently, the Aerodyne AMS has been deployed widely in China (particularly  
109 Beijing) (e.g., Xu et al., 2014 and references therein;Sun et al., 2014;Yeung et al.,  
110 2014;Zhang et al., 2014;Li et al., 2015;Shen et al., 2015;Sun et al., 2015a;Sun et al.,  
111 2015b;Yan et al., 2015;Zhang et al., 2015;Tang et al., 2016;Zhang et al., 2016a;Jiang  
112 et al., 2015;Chen et al., 2015;Xu et al., 2015;Du et al., 2015;Sun et al., 2016;Wang et  
113 al., 2015;Han et al., 2015;Wang et al., 2016b). However, only a few field campaigns  
114 were conducted in the YRD region. Huang et al. (2012b) deployed an HR-ToF-AMS  
115 together with an SP2 in Shanghai during the 2010 Shanghai World Expo, and in

116 Jiaying during summer and winter of 2010 (Huang et al., 2012a). In urban Nanjing, an  
117 ACSM was applied for characterizing  $PM_{10}$  during summer and autumn harvest  
118 seasons (Zhang et al., 2015), and during December 2013 to investigate a few heavy  
119 haze events (Zhang et al., 2016b). In addition, a Q-AMS was deployed in Nanjing to  
120 investigate the effects of  $PM_{10}$  on visibility during January 2013 (Shen et al., 2015).  
121 Furthermore, a recent study by Wang et al. (2016a) reported the observation of  
122 fullerene soot in suburban Nanjing using an SP-AMS. Nevertheless, many questions  
123 remain unclear with regard to aerosol chemistry, sources, and processes in this region.  
124 Moreover, none of the previous AMS measurements studied the aerosol  
125 characteristics during springtime in Nanjing, yet the springtime aerosols may have  
126 different behaviors than those in other seasons, when aerosols are likely influenced  
127 significantly by emissions from biomass burning, coal burning etc. For these reasons,  
128 we reports in this work the real-time measurement results on urban fine aerosols in  
129 Nanjing using the SP-AMS during spring in 2015. The rich highly-time resolved,  
130 highly-chemical resolved mass spectral data, as well as chemically-resolved size  
131 distributions of different aerosol species obtained for the first time in Nanjing during  
132 this study, can allow us to conduct in-depth analyses, and better understand the  
133 characteristics, sources and relevant transformation processes of ambient aerosols.  
134 The findings for such a megacity are also valuable to the Pan-Eurasian Experiment  
135 (PEEX) infrastructure which aims to resolve the major uncertainties in Earth system  
136 science and global sustainability issues (Kulmala et al., 2015).

137

## 138 **2. Experiments**

### 139 **2.1 Sampling site and instrumentation**

140 The field campaign was conducted in the environment monitoring station of  
141 Nanjing Olympic center ( $32^{\circ}0'33.00''N$ ,  $118^{\circ}44'9.53''E$ , Fig. S1) from April 13 to 29,  
142 2015. Details of the sampling site are shown in Fig. S1. The site was surrounded by  
143 residential buildings, close to a few urban arterial roads ( $\sim 85$  m northwest of  
144 Huangshan Road,  $\sim 200$  m northeast to Mengdu Street and  $\sim 425$  m southwest of

145 Xinglong Street). There are also a restaurant (~50 m), a student cafeteria (~300 m),  
146 and the Nanjing Cigarette Factory (~480 m southeast) around the site.

147 The sampling inlet was installed outside the fifth floor of the building (~12 m  
148 above the ground), with a PM<sub>2.5</sub> cyclone (URG Corp., Chapel Hill, NC, USA) to  
149 remove coarse particles. Ambient particles were dried (RH <10%) via a diffusion  
150 dryer filled with silica gel before entering into the SP-AMS. The sampling line (~2 m  
151 long) was assembled using stainless steel tubing and proper fittings. Air flow was  
152 controlled at around ~5 L min<sup>-1</sup>, with a flow rate into the SP-AMS at ~80 cm<sup>3</sup> min<sup>-1</sup>.

153 The SP-AMS can measure non-refractory (NR) PM<sub>1</sub> components including  
154 ammonium, nitrate, sulfate, chloride and organics similar to other types of AMS via a  
155 thermal tungsten heater. Moreover, it can also measure *r*BC and inorganic/organic  
156 species that coated on the *r*BC cores, as it is equipped with an intracavity Nd:YAG  
157 laser vaporizer (1064 nm) (Onasch et al., 2012). During this campaign, the instrument  
158 was switched between “laser on” and “laser off” settings, and between V-mode (better  
159 for mass quantification) and W-mode (better chemical resolution, ~5000 in this study),  
160 with one cycle including six menu settings (M1: Laser on V-mode; M2: Laser off  
161 V-mode; M3: Laser on W-mode; M4: Laser off W-mode; M7: Laser on PToF-mode;  
162 M8: Laser off PToF-mode). Each menu was set to 2.5 min, thus a full running cycle  
163 lasted for 15 mins. The PToF-mode was under V-mode, but was tuned in particular  
164 for measuring particle sizes. The tungsten heater was always turned on and kept at  
165 ~600°C.

166 The SP-AMS, in conjunction with a scanning mobility particle sizer (SMPS) (TSI  
167 inc., Shoreview, MN, USA) was calibrated for mass quantification (e.g., ionization  
168 efficiency) using size-selected (250 nm and 300 nm) monodisperse ammonium nitrate  
169 particles following the procedures detailed in Jimenez et al. (2003). Pure ammonium  
170 sulfate was used to determine the relative ionization efficiency (RIE) of sulfate  
171 (Setyan et al., 2012). Quantification of *r*BC was calibrated using Regal Black  
172 (REGAL 400R pigment black, Cabot Corp.) particles according to the procedures  
173 reported in Onasch et al. (2012). Note that the solution of Regal Black was sonicated

174 during calibration to maintain a relative stable aerosol flow. RIEs of ammonium,  
175 nitrate, sulfate, chloride, organics and *r*BC were determined to be 3.15, 1.05, 1.20, 1.3,  
176 1.4 and 0.33, respectively. On the other hand, particle sizing was calibrated using  
177 standard polystyrene latex (PSL) spheres (Duke Scientific Corp., Palo Alto, CA, USA)  
178 across 100 - 700 nm range. Flow rate was also calibrated prior to the measurement.

179 Concentrations of gaseous species, e.g., carbon monoxide (CO) (Model T300,  
180 Teledyne API, USA), ozone (O<sub>3</sub>) (Model EC9810, Ecotech Pty Ltd, Australia),  
181 nitrogen dioxide (NO<sub>2</sub>) and sulfur dioxide (SO<sub>2</sub>) (Model LGH-01, Anhui Landun,  
182 China), and meteorological data including air temperature (T), relative humidity (RH),  
183 visibility (km), wind speed (WS) and wind direction (WD) were acquired at the same  
184 site. PM<sub>2.5</sub> and PM<sub>10</sub> mass concentrations were also recorded (BAM-1020, Met One  
185 Instruments, Inc., USA), in parallel with the SP-AMS measurement.

## 186 **2.2 Data treatment and source analyses**

187 The SP-AMS data were post-processed by using the Igor-based standard  
188 ToF-AMS Analysis Toolkit SQUIRREL v1.56D and PIKA v1.15D, available at:  
189 <http://cires1.colorado.edu/jimenez-group/ToFAMSResources/ToFSoftware/index.htm>  
190 1. Note all mass concentrations reported here were calculated from the HR fitted  
191 results on V-mode data. A collection efficiency is typically used to account for the  
192 particles that aren't collected and measured by the instrument, due to the particles lost  
193 during passage through inlet, time-of-flight chamber and bouncing from the vaporizer.  
194 For the SP-AMS, the CE of laser vaporizer is mainly governed by particle divergence,  
195 while for the tungsten vaporizer, the CE is governed mainly by the bouncing effects  
196 (Matthew et al., 2008). A CE value of 0.5 is valid and used commonly for the AMS  
197 measurements for most environments (Canagaratna et al., 2007). Nevertheless,  
198 Middlebrook et al. (2012) further investigated this issue, and found that high aerosol  
199 acidity, high ammonium nitrate, and high sampling line RH can increase the CE, and  
200 provide composition-dependent CE parametrization. For our dataset, we found that  
201 the composition-dependent CE rather than a constant CE=0.5 has negligible effects on  
202 the quantification of aerosol species, as the particles were neutralized (Fig. 3a), the

203 mass fraction of ammonium nitrate were <40% in almost all cases, and also the  
204 sampling line RH was below 10%. And in fact, the PM<sub>1</sub> mass concentrations  
205 quantified by using the composition-dependent CE correlate a bit worse with the  
206 PM<sub>2.5</sub> concentrations than ones using CE=0.5. Thus, we a constant CE of 0.5, in  
207 consistent with many other AMS studies, was employed for this dataset.

208 Unless specified, the concentrations of ammonium, sulfate, nitrate, chloride and  
209 organics are from M2 setting (tungsten vaporizer only), while the *r*BC data is from  
210 M1 setting (dual-vaporizers: tungsten + laser) in this paper. The meteorological data  
211 (RH, T, WS, WD and visibility), concentrations of gas-phase species (CO, NO<sub>2</sub>, SO<sub>2</sub>  
212 and O<sub>3</sub>) and PM<sub>2.5</sub> were averaged into hourly data for comparisons with the SP-AMS  
213 data. The data reported are at local time, e.g., Beijing (BJ) Time.

214 Positive matrix factorization (PMF) (Paatero and Tapper, 1994) was applied on  
215 the high resolution mass spectra (HRMS) of organic aerosol (OA) obtained under  
216 laser off W-mode (M4 setting) to elucidate the OA sources/processes. We used the  
217 PMF Evaluation Tool version 2.08A (downloaded from:  
218 [http://cires1.colorado.edu/jimenez-group/wiki/index.php/PMF-AMS\\_Analysis\\_Guide](http://cires1.colorado.edu/jimenez-group/wiki/index.php/PMF-AMS_Analysis_Guide))  
219 (Ulbrich et al., 2009) to investigate the PMF results by varying the number of factors  
220 (from 2 to 8 factors) and rotations (“*f*peak”, from -1 to 1 with an increment of 0.1).  
221 Only ions with *m/z* less than or equal to 180 were included in the analyses. Following  
222 the instruction detailed by Zhang et al. (2011), the 4-factor solution (at *f*peak = -0.1)  
223 was chosen as the optimal solution, as the 3-factor solution cannot separate the  
224 hydrocarbon-like OA (HOA) and cooking OA (COA) (Fig. S2). For the 5-factor  
225 solution (Fig. S3), Factor 2 and Factor 4 are clearly a split from the SVOOA from the  
226 4-factor solution ( $r^2 = 0.89$  and slope of 1.05); Factor 2 of 5-factor solution also shows  
227 much weaker correlations with nitrate than SVOOA of 4-factor solution does ( $r =$   
228 0.07 vs. 0.49). A summary of the key diagnostic plots are provided in Fig. S4.  
229 Detailed discussion of the PMF results is presented in Section 3.5. Note we found no  
230 significant differences between the PMF source apportionment results from the  
231 HRMS of OA (without *r*BC) obtained with dual-vaporizers setting (M3 setting) and



232 current results (M4 setting, tungsten vaporizer only), as the OA HRMS acquired under  
233 these two circumstances were overall very similar (details in Section 3.4).

234 Note the elemental ratios shown throughout the paper were all calculated based  
235 on the method proposed by Aiken et al. (2008) (referred to as A-A method). Recently,  
236 Canagaratna et al. (2015) improved this methodology by using specific ion fragments  
237 as markers to calculate the O/C and H/C ratios (referred to as I-A method). The I-A  
238 method increased the O/C ratio, H/C ratio, and the OM/OC ratio from the values  
239 calculated from the A-A method, on average, by 28%, 10% and 8%, respectively (Fig.  
240 S5). In this work, we used the results from the A-A method for consistency and  
241 comparisons with previous AMS measurements.

242

### 243 **3. Results and discussion**

#### 244 **3.1 Mass concentrations, chemical compositions and diurnal changes**

245 The temporal variations of meteorological parameters, concentrations of the gas  
246 pollutants, concentrations and mass fractions of different PM<sub>1</sub> components, and the  
247 PM<sub>2.5</sub> mass loadings (from Met one BAM-1020) over the sampling period are  
248 illustrated in Fig. 1. During this study, the mean temperature was 18.5 °C, RH on  
249 average was 64%, and wind predominantly blew from southeast and southwest (Fig.  
250 S6). The SP-AMS PM<sub>1</sub> concentrations ranged from 5.1 to 97.9 μg m<sup>-3</sup>, with an  
251 average of 28.2 μg m<sup>-3</sup>. Note this average PM<sub>1</sub> concentration is significantly lower  
252 than those observed during summer (38.5 μg m<sup>-3</sup>), autumn (46.4 μg m<sup>-3</sup>) and winter  
253 (89.3 μg m<sup>-3</sup>) (Zhang et al., 2015; Zhang et al., 2016b), showing that the air during  
254 springtime in Nanjing is cleaner than in other seasons. The variations of PM<sub>1</sub>  
255 concentrations also match very well with PM<sub>2.5</sub> concentrations (Pearson's  $r^2 = 0.72$ ),  
256 and on average PM<sub>1</sub> accounts for ~ 54% of the PM<sub>2.5</sub> mass. This ratio appears to be a  
257 bit low, likely due to the uncertainty of CE of the SP-AMS.

258 The average PM<sub>1</sub> composition is shown in Fig. 2a. The most abundant component  
259 is found to be organics (45.0%), following by sulfate (19.3%), nitrate (13.6%),  
260 ammonium (11.1%), rBC (9.7%) and chloride (1.3%). Fig. 2b further shows changes

261 of the PM<sub>1</sub> chemical compositions in different concentration bins. It can be seen that  
262 although most PM<sub>1</sub> mass loadings are within 10 - 40 μg m<sup>-3</sup>, high loading periods tend  
263 to have higher mass contributions from organics and rBC, and less contributions from  
264 secondary inorganic species, indicating that high PM events were influenced  
265 significantly by local fresh emissions.

266 The molar ratio of inorganic anions (sulfate, nitrate and chloride) to cations  
267 (ammonium) is 1.05 (Fig. 3a) (Zhang et al., 2007b). Considering that a small fraction  
268 of sulfate, nitrate and chloride are possibly associated with metal cations, such as Na<sup>+</sup>,  
269 K<sup>+</sup> and Ca<sup>2+</sup>, etc., it can be concluded that the NR-PM<sub>1</sub> was overall neutral throughout  
270 the study. On the other hand, the molar ratio of inorganic anions to ammonium is on  
271 average 1.17 (Fig. 3b) when dual-vaporizers are on. This may be partially due to  
272 variations of ionization/collection efficiencies of the measured species as the addition  
273 of laser beam may change the distribution of vaporized species inside the ion chamber,  
274 and also because of the detection of sulfate, nitrate and chloride bonded with metal  
275 cations under the dual-vaporizers. These species don't evaporate on the tungsten  
276 vaporizer under the laser-off mode. Indeed, more metal signals were observed with  
277 the dual-vaporizers, as shown in Fig. S7.

278 Fig. 2c shows the average diurnal changes of organics, sulfate, nitrate, chloride  
279 and rBC. Sulfate concentrations are slightly higher during daytime than during  
280 nighttime, indicating a significant contribution from photochemical reactions. Sulfate  
281 also shows the least variations among all species, reflecting its regional behavior.  
282 Except for sulfate, all other species present a dual-peak pattern, with one peak in early  
283 morning and another one in early evening. The peaks of rBC and organics are likely  
284 due to local traffic/cooking activities (see details in Section 3.5), while the behavior of  
285 nitrate is likely driven by the thermodynamic gas-particle partitioning: NH<sub>3</sub>(g) +  
286 HNO<sub>3</sub>(g) ↔ NH<sub>4</sub>NO<sub>3</sub>(p) as it shows good anti-correlations with the diurnal changes  
287 of temperatures ( $r = -0.72$  for nitrate vs. T). The good correlations between the diurnal  
288 cycles of nitrate and RH, in particular during nighttime, suggest a nighttime formation  
289 pathway of nitrate, e.g., N<sub>2</sub>O<sub>5</sub> + H<sub>2</sub>O = 2HNO<sub>3</sub> and HNO<sub>3</sub> + NH<sub>3</sub> = NH<sub>4</sub>NO<sub>3</sub>.

290 Furthermore, we calculated the diurnal variations of the equilibrium constant of  
291  $\text{NH}_4\text{NO}_3$  ( $K_{p,AN}$ ) (Seinfeld and Pandis, 2006; Young et al., 2016) in Fig. 2c. The  $K_{p,AN}$   
292 displays a similar trend as nitrate ( $r = 0.68$ ), providing strong evidence that nitrate  
293 variations were governed mainly by the thermodynamic equilibrium. Chloride shows  
294 similar behavior as nitrate, indicating it is driven by the equilibrium  $\text{NH}_3(\text{g}) + \text{HCl}(\text{g})$   
295  $\leftrightarrow \text{NH}_4\text{Cl}(\text{p})$  as well ( $r = -0.76$  for chloride vs. T). Therefore, when temperature rises,  
296 more  $\text{NH}_4\text{NO}_3$  and  $\text{NH}_4\text{Cl}$  can dissociate into gaseous  $\text{NH}_3$ ,  $\text{HNO}_3$  and  $\text{HCl}$ , mass  
297 loadings of particle-phase nitrate and chloride decrease correspondingly, and *vice*  
298 *versa*.

299 In order to further elucidate the formation processes of sulfate, we calculated the  
300 oxidation ratios of sulfur ( $f_s$ ) (Fig. 4a), defined as  $f_s = n\text{SO}_4^{2-} / (n\text{SO}_4^{2-} + n\text{SO}_2)$  (Xu et  
301 al., 2014), indicating the conversion of  $\text{SO}_2$ . Here  $n\text{SO}_4^{2-}$  and  $n\text{SO}_2$  are the molar  
302 quantities of particle-phase sulfate, and gas-phase  $\text{SO}_2$ , respectively. Diurnal  
303 variations of  $f_s$  and RH are presented in Fig. 4b, and Fig. 4c shows variations of sulfate  
304 and nitrate concentrations with RH. The diurnal profile of  $f_s$  shows a negative  
305 correlation with that of RH ( $r = -0.52$ ), and mass concentrations of sulfate even drop  
306 under high RH conditions, indicating an insignificant role of aqueous-phase  
307 processing for sulfate formation during this campaign. On the other hand, the  $f_s$   
308 reaches a maximum around 3 pm. Note the afternoon rise of  $f_s$  and sulfate may be  
309 affected by the down mixing of sulfate formed earlier, however, since concentrations  
310 of all other aerosol species that mix with sulfate decrease significantly, we postulate  
311 that the increase of  $f_s$  likely suggest the photochemical production of sulfate in the  
312 afternoon.

313

### 314 **3.2 Chemically-resolved size distributions**

315 The campaign-averaged mass-based size distributions, fractional contributions  
316 and diurnal size distributions (image plots) of the major  $\text{PM}_{10}$  species are depicted in  
317 Fig. 5 (temporal variations of the mass-based size distributions of these  $\text{PM}_{10}$  species  
318 over the whole measurement period are provided in Fig. S8). Note the size

319 distribution of *r*BC in these plots were scaled from the size distribution of  $m/z$  24  
320 ( $C_2^+$ ), as other major *r*BC ion clusters may be heavily influenced by other ions, such  
321 as  $C^+$  signal but from organics at  $m/z$  12 ( $C^+$ ),  $HCl^+$  signal at  $m/z$  36 ( $C_3^+$ ),  $SO^+$  signal  
322 at  $m/z$  48 ( $C_4^+$ ),  $C_2H_4O_2^+$  signal at  $m/z$  60 ( $C_5^+$ ). It also should be note that, although  
323 the AMS is able to capture the bulk of atmospheric accumulation mode particles  
324 (Canagaratna et al., 2007), right side of size distributions may be affected by the  
325 incomplete transmission of larger particles limited by the SP-AMS inlet (in particular,  
326 the supermicron ones).

327 As can be expected, all inorganic species (sulfate, nitrate, chloride and  
328 ammonium) display a unimodal distribution with an accumulation mode peaking  
329  $\sim 550$  nm (vacuum aerodynamic diameter,  $D_{va}$  (DeCarlo et al., 2004)), since they were  
330 mainly formed from secondary reactions. The organics has a much broader size  
331 distribution across from ultrafine ( $<100$  nm) to supermicron meter range, with a small  
332 sub-peak centering  $\sim 120$  nm in addition to the major peak at  $\sim 440$  nm, indicating  
333 influences from both primary and secondary emissions. On the contrary, size  
334 distribution of *r*BC behaves very differently from other components, which peaks at  
335 90 - 200 nm range, reflecting clearly that it is mainly originated from primary  
336 emissions. Overall, the small particles are predominantly consisted of organics and  
337 *r*BC, which together account for more than 90% of the ultrafine particle mass. Mass  
338 contributions from inorganic species increase significantly with the increase of  
339 particle size, and they dominate masses of particles larger than 400 nm (Fig. 5b).

340 In line with the diurnal mass loadings of the  $PM_{10}$  species shown in Fig. 2c, the  
341 diurnal size distribution of sulfate is generally stable, with masses concentrating in the  
342 400 - 700 nm range throughout the day (Fig. 5c); while the size distributions of nitrate,  
343 chloride and organics present clear enhancements in the 300 - 700 nm range during  
344 early morning and early evening due to increased mass concentrations of these species  
345 during these two periods. The size distribution of *r*BC is also enhanced during the  
346 morning and evening hours, but it extends to a much smaller size range ( $<100$  nm).

347

### 348 3.3 PM<sub>1</sub> contributions on visibility impairment

349 In order to figure out the major species that are responsible for the visibility  
350 degradation, here we employed the IMPROVE method to reconstruct the light  
351 extinction coefficients ( $b_{\text{ext}}$ ).  $b_{\text{ext}}$  values are derived from the measured visibility:  
352  $b_{\text{ext}}=3.91/V_s$  (Kong et al., 2015), where  $V_s$  stands for the visibility (in meter). The  
353 following IMPROVE formula (Yang et al., 2007) was used:

$$354 \quad b_{\text{ext}} = 3f(\text{RH})\{[(\text{NH}_4)_2\text{SO}_4] + [\text{NH}_4\text{NO}_3] + [\text{NH}_4\text{Cl}]\} + 4[\text{OM}] + 10[\text{BC}] + 1[\text{soil}] + 10$$

355 Where  $f(\text{RH})$  is a RH-dependent empirical coefficient which considers the effects of  
356 water uptake by inorganic salts on the light extinction; the  $f(\text{RH})$  values used here  
357 were taken from Malm and Day (2001), which were regressed from the Great Smoky  
358 data set.  $[(\text{NH}_4)_2\text{SO}_4]$ ,  $[\text{NH}_4\text{NO}_3]$ ,  $[\text{NH}_4\text{Cl}]$ ,  $[\text{OM}]$ , and  $[\text{BC}]$  represent the mass  
359 concentrations of ammonium sulfate, ammonium nitrate, ammonium chloride,  
360 organics and black carbon directly from the SP-AMS measurements (in  $\mu\text{g m}^{-3}$ )  
361 ( $[(\text{NH}_4)_2\text{SO}_4] = 1.375*[\text{SO}_4^{2-}]$ ,  $[\text{NH}_4\text{NO}_3]=1.29*[\text{NO}_3^-]$  and  $[\text{NH}_4\text{Cl}] = 1.51*[\text{Cl}^-]$ ).  
362 Since the SP-AMS cannot accurately measure soil components (e.g., various  
363 metals/metal oxides/metal salts), the term  $[\text{soil}]$  was set to zero during calculations.

364 By using this method, the reconstructed visibilities match reasonably well with  
365 the measured values ( $r^2 = 0.50$ ) as shown in Fig. 6a. Fig. 6b shows the time series of  
366 the measured and reconstructed extinction coefficients throughout the whole sampling  
367 period. It should be noted that, on average, the measured PM<sub>1</sub> species are only able to  
368 explain ~44% of the light extinction. This is likely due to that: 1) as shown earlier, the  
369 SP-AMS measured PM<sub>1</sub> only occupies ~54% of the PM<sub>2.5</sub> mass; 2) we didn't include  
370 contributions from soil components, coarse particles and also some gas-phase species  
371 (such as NO<sub>2</sub>); 3) although the influences of water are included in part through  $f(\text{RH})$   
372 for inorganic salts, the water uptake by organic species are not considered explicitly,  
373 which can be significant especially for the SOA under high RH conditions (Duplissy  
374 et al., 2011; Denjean et al., 2015). Indeed, as shown in Fig. 6a, reconstructed  
375 visibilities appear to deviate more significantly from the measured visibilities under  
376 high RH than ones under low RH conditions, suggesting the importance of

377 particle-bounded water on visibility degradation. The pie chart in Fig. 6b presents the  
378 average relative contributions of different components to the light extinction of PM<sub>1</sub>.  
379 The largest contributor is organics which accounts for 37.7%, followed by ammonium  
380 sulfate (25.1%), *r*BC (20.7%), ammonium nitrate (15.1%) and a minor contributor of  
381 ammonium chloride (1.4%).

382

### 383 **3.4 Chemical characteristics of OA**

384 The unique laser vaporizer of SP-AMS allows it to detect *r*BC and species coated  
385 on the *r*BC core including both non-refractory and refractory organics, thus  
386 comparison between the OA mass spectra obtained with dual-vaporizers and tungsten  
387 vaporizer settings, can infer some information regarding the chemical features of  
388 refractory organics, which were unable to be determined by any other types of AMS.  
389 As shown in Fig. 7a and 7b, the OA obtained with dual-vaporizers setting have  
390 slightly higher oxygen-to-carbon (O/C) ratio (0.28 vs. 0.27), nitrogen-to-carbon (N/C)  
391 ratio (0.033 vs. 0.032) and lower hydrogen-to-carbon (H/C) ratio (1.50 vs. 1.52) than  
392 the corresponding elemental ratios of OA obtained with the tungsten vaporizer only.  
393 This result indicates that refractory organics are likely more oxygenated than the  
394 non-refractory organics, and for this dataset it is mainly due to a higher fractional  
395 contribution from C<sub>2</sub>H<sub>3</sub>O<sup>+</sup> (see the inset of Fig. 7a). This is different from the results  
396 on laboratory-generated nascent soot, where larger *f*CO<sub>2</sub><sup>+</sup> (i.e., the fraction of total  
397 organic signal contributed by CO<sub>2</sub><sup>+</sup>) was observed with the dual-vaporizers setting,  
398 indicating the variability of the chemical compositions of refractory organics.

399 It should be noted that, accurate determination of refractory organics is very  
400 difficult, because: 1) A large portion of refractory organics cannot be detected by the  
401 SP-AMS if they didn't coat on *r*BC cores; 2) To accurately measure the species only  
402 coated on *r*BC cores, the tungsten vaporizer has to be physically removed, otherwise  
403 the vaporizer temperature is still around 150°C even its power is turned off, and the  
404 non-refractory organics that don't coat on *r*BC cores can still be measured, and  
405 complicates the analyses; 3) The CE and IE values for different species may vary

406 under different vaporizer settings, so that direct subtraction of organics measured  
407 under tungsten-only setting from the organics measured under dual-vaporizer setting  
408 may not represent the real refractory organics; 4) Some ions measured under  
409 dual-vaporizer setting are likely induced by the laser itself rather than the 70 eV  
410 electron impact. For example, a series of fullerene-like carbon clusters can be  
411 generated by the laser itself, even though they don't really exist in the atmosphere  
412 (Wang et al., 2016a; Onasch et al., 2015). This laser-induced ion formation scheme  
413 may work for other organics, thus makes it even more difficult for identifying the  
414 refractory organics. Further studies are essential to investigate this issue.

415 Overall, the O/C ratio (0.27) of OA in Nanjing during springtime is a bit lower  
416 than those observed at other urban locations in China – for instances, 0.30 in  
417 Shenzhen (He et al., 2011), 0.31 in Shanghai (Huang et al., 2012b), 0.33 in Lanzhou  
418 (Xu et al., 2014) and 0.34 in Beijing (Zhang et al., 2014), and much lower than those  
419 at rural sites – for instances, 0.47 in Kaiping (Huang et al., 2011) and 0.59 in  
420 Changdao (Hu et al., 2013). As O/C ratio is a good indicator of the aging degree of  
421 OA, the relatively low O/C level indicates a significant contribution from fresh  
422 emissions in Nanjing aerosols during springtime. Accordingly, the non-refractory OA  
423 (pie chart in Fig. 7b) is dominated in hydrocarbon  $C_xH_y^+$  ions (51.2%) rather than the  
424 oxygen-containing ion fragments (37.4% of  $C_xH_yO_1^+$  and  $C_xH_yO_2^+$ ).

425 The scatter plot of  $f_{44}$  (mass fraction of  $m/z$  44 to the total OA) vs.  $f_{43}$  (mass  
426 fraction of  $m/z$  43 to the total OA) (a.k.a., triangle plot) (Ng et al., 2010) was often  
427 used to investigate the oxidation degrees of OA. As presented in Fig. 8, most OA  
428 reside in the bottom end of the triangular region, again pointing out the  
429 less-oxygenated behavior of the OA. Since the HRMS can separate different ions at  
430 the nominal  $m/z$ , we also examined the  $f_{CO_2^+}$  vs.  $f_{C_2H_3O^+}$  space and illustrated it in  
431 Fig. S9 - many OA locate outside the triangular region, yet still close to the bottom.  
432 Moreover,  $m/z$  60 (mainly  $C_2H_4O_2^+$ ) is a significant fragment ion of levoglucosan,  
433 which is well known as the biomass burning aerosol tracer (Alfarra et al., 2007).  
434 However, as  $f_{60}$  (mass fraction of  $m/z$  60 to the total OA) is very low in OA (average

435  $\pm 1\sigma = 0.4 \pm 0.06 \%$ ), indicating no biomass burning influences on the OA properties  
436 during springtime in Nanjing.

437

### 438 **3.5 Sources and evolution processes of OA**

439 In order to further elucidate the sources and evolution processes of OA, we  
440 performed PMF analyses and identified four OA components, including two primary  
441 OA (POA) factors – a traffic-related hydrocarbon-like OA (HOA) and a  
442 cooking-related OA (COA), and two secondary OA factors – a semi-volatile  
443 oxygenated OA (SV-OOA) and a low volatility OOA (LV-OOA). Details about their  
444 characteristics are discussed below.

#### 445 **3.5.1 Mass spectral features of the OA factors**

446 The mass spectral profiles, time-dependent mass concentrations of the four OA  
447 factors and corresponding tracer ions are presented in Fig. 9. The HOA mass spectrum  
448 is overall dominated by the  $C_xH_y^+$  ions (73.2%), such as  $C_3H_7^+$ ,  $C_4H_7^+$ ,  $C_4H_9^+$ ,  $C_5H_9^+$   
449 etc., which are most likely produced from alkanes and cycloalkanes emitted from fuel  
450 and lubricating oil burning (Canagaratna et al., 2004). This feature is in good  
451 agreement with the mass spectral features of POA directly from vehicle  
452 emissions (Collier et al., 2015), and the HOA factors determined in many other  
453 locations (e.g., Ge et al., 2012b; Huang et al., 2010; Sun et al., 2011). HOA has the  
454 lowest O/C ratio (0.10) and highest H/C ratio (1.75) among all factors, representing its  
455 behavior as primary fresh emissions. The COA mass spectrum is also rich in  $C_xH_y^+$   
456 ions (64.7%), but having more oxygenated ions ( $C_xH_yO_z^+$ ) than the HOA (26.5% vs.  
457 15.4%), especially  $C_3H_3O^+$  and  $C_3H_5O^+$  ions. The significant contributions of  $C_3H_3O^+$   
458 and  $C_3H_5O^+$  to  $m/z$  55 and  $m/z$  57 are a common feature of COA, that has been  
459 reported in various urban locations around the world, for examples, Beijing (Sun et al.,  
460 2015a), London (Allan et al., 2010), Fresno (Ge et al., 2012b), New York City (Sun et  
461 al., 2011) and Barcelona (Mohr et al., 2012; Mohr et al., 2015). These  
462 oxygen-containing ions are in part generated from the fragmentation of fatty acids in  
463 the cooking aerosols (Ge et al., 2012b). As a result, COA has a higher O/C ratio of



464 0.16 and a lower H/C ratio of 1.67 than those of HOA. The O/C and H/C levels of  
465 COA in this work are also close to those identified in other locations aforementioned.  
466 The consistency of the chemical characteristics of COA from such different locations  
467 suggests that ambient COA is more relevant to the cooking oil rather than the different  
468 types of food, which was postulated earlier by Allan et al. (2010).

469 Unlike the two POA factors, SV-OOA and LV-OOA are both abundant in  
470 oxygen-containing fragments ( $C_xH_yO_z^+$  ions), which are 46.4% and 54.8%,  
471 respectively. The higher O/C ratio (0.55 vs. 0.32) and more  $C_xH_yO_2^+$  ions (18.8% vs.  
472 11.8%) in the LV-OOA mass spectrum than those of the SV-OOA, reflecting the fact  
473 that LV-OOA went through more aging/oxidation reactions than SV-OOA. The O/C  
474 ratio of SV-OOA is 0.32, which is within the O/C range of SV-OOA observed  
475 worldwide (Jimenez et al., 2009). The LV-OOA O/C ratio of 0.55 is in the lower end  
476 compared to the O/C levels of LV-OOA observed in other China sites, for examples,  
477 0.64 in Kaiping (Huang et al., 2011), 0.65 in Shanghai (Huang et al., 2012b), 0.68 in  
478 Lanzhou (Xu et al., 2014), 0.78 in Changdao (Hu et al., 2013) and 0.80 in Hong Kong  
479 (Lee et al., 2013).

480 Consistently, in the  $f_{44}$  vs.  $f_{43}$  space (Fig. 8), SV-OOA situates near the bottom  
481 side while LV-OOA approaches to the upper part of the triangular region, because of a  
482 much larger fractional contribution of  $CO_2^+$  in the LV-OOA mass spectrum. HOA and  
483 COA, as POA factors, both reside in the bottom end of the plot, away from SV-OOA  
484 and LV-OOA; while they locate outside the triangle in the  $f_{CO_2^+}$  vs.  $f_{C_2H_3O^+}$  space  
485 (Fig. S9), indicating that the HRMS acquired by the SP-AMS is better in  
486 differentiating POA factors from other SOA factors than the unit mass resolution  
487 (UMR) data.

488 In order to justify the OA factors identified in this study, we compared the  
489 spectral similarities of the OA factor spectral profiles (in both HR and UMR) with  
490 those separated during wintertime in Beijing (Sun et al., 2015a), summertime in  
491 Lanzhou (Xu et al., 2014), and wintertime in Fresno (Ge et al., 2012b; Ge et al.,  
492 2012a). The results are listed in Table 1. Indeed, the HOA, COA and LV-OOA mass

493 spectra are highly similar to the corresponding factors identified in Beijing, Lanzhou  
494 and Fresno ( $r^2 > 0.87$ ); SV-OOA also correlates fairly well with Beijing and Lanzhou  
495 SV-OOA too, but with relative low  $r^2$  (0.68 – 0.75), mainly because of one or two ion  
496 fragments, namely, higher  $\text{CO}^+$  and  $\text{CO}_2^+$  signals in Beijing SV-OOA and higher  
497  $\text{C}_2\text{H}_3\text{O}^+$  signal in Lanzhou SV-OOA than those in Nanjing SV-OOA. The SV-OOA on  
498 the other hand, correlates very well with the Fresno OOA ( $r^2 = 0.90$  and  $0.91$ ).

499 Moreover, as presented in Fig. 9a, the HOA mass spectrum contains relatively  
500 higher fraction of ions with large  $m/z$  values ( $m/z > 100$ ) than that of COA (14.0% vs.  
501 8.2%), and most of these ions are  $\text{C}_x\text{H}_y^+$  ions, probably from fuel burning emitted  
502 long-chain alkanes, etc. The SV-OOA also includes more large  $m/z$  ion fragments ( $m/z >$   
503 100) than those in the LV-OOA mass spectrum (10.5% vs. 5.3%), likely suggesting  
504 that further oxidation of SOA species may lead to the fragmentation of high molecular  
505 weight species and formation of small molecules – a mechanism verified by both  
506 lab-scale experiments (e.g., Yu et al., 2014) and field measurements (e.g., Lee et al.,  
507 2012).

### 508 **3.5.2 Temporal variations, diurnal patterns and relative contributions of the OA** 509 **factors**

510 The temporal variations of different OA factors and their corresponding tracer  
511 ions are displayed in Fig. 9b.  $\text{C}_4\text{H}_9^+$  ion, a.k.a., the HOA mass spectral tracer (Zhang  
512 et al., 2005) indeed varies very closely to the HOA ( $r^2 = 0.94$ ). Time series of the COA  
513 tracer ion  $\text{C}_6\text{H}_{10}\text{O}^+$  (and also  $\text{C}_5\text{H}_8\text{O}^+$ ,  $\text{C}_7\text{H}_{12}\text{O}^+$ ) (Sun et al., 2011; Ge et al., 2012b)  
514 match very well with that of COA too ( $r^2 = 0.90$ ). SV-OOA correlates better with  
515  $\text{C}_2\text{H}_3\text{O}^+$  ( $r^2 = 0.90$ ) than with  $\text{CO}_2^+$  ( $r^2 = 0.66$ ). Although LV-OOA doesn't correlate  
516 very well with  $\text{CO}_2^+$  ( $r^2 = 0.12$ ) mainly due to the mismatch during April 23 - 26, the  
517 correlation is still much better than it with  $\text{C}_2\text{H}_3\text{O}^+$  ( $r^2 < 0.001$ ). In Table 2, we  
518 tabulate the correlation coefficients ( $r$ ) of the four OA factors with the gas-phase  
519 species, BC and inorganic species. Note we used Pearson's  $r$  not  $r^2$  here since some  
520 correlation coefficients are negative. From the table, it is clear that the traffic-related  
521 gaseous species, CO and  $\text{NO}_2$ , correlate best with HOA among all OA factors;

522 SV-OOA correlates better with nitrate ( $r = 0.49$ ) than it with sulfate ( $r = 0.11$ );  
523 LV-OOA correlate better with sulfate ( $r = 0.23$ ) than it with nitrate ( $r = 0.11$ ). All these  
524 results are consistent with the traffic origin of HOA, the semi-volatile and  
525 low-volatility behaviors of SV-OOA and LV-OOA.

526 Accordingly, diurnal cycles of the OA factors are presented in Fig. 10a.  
527 Correlation coefficients ( $r$ ) of the diurnal variations between OA factors with  
528 gas-phases and inorganic species are provided in Table 2, as well. HOA  
529 concentrations show an early morning peak, and it overall remains at high levels  
530 during nighttime. Besides the impacts of boundary layer height, this is also due to  
531 enhanced emissions from construction vehicles around the site, which were in fact  
532 much more active during nighttime than during daytime because of the restrictions of  
533 Nanjing government. Most of those vehicles used low-quality diesel fuel, and could  
534 emit a large amount of  $r$ BC particles. The  $r$ BC diurnal pattern is indeed almost  
535 identical to that of HOA ( $r = 0.99$ ), indicating that the HOA during this campaign was  
536 apparently associated with the construction vehicle emissions. COA concentrations  
537 increase during noon (12 pm – 1 pm) and early evening, in response to the lunchtime  
538 and dinnertime cooking activities. SV-OOA concentrations decrease from 9 am, and  
539 reach a minimum during afternoon (3 pm – 4 pm), oppositely to the variation of  
540 temperatures ( $r = -0.85$ ) but similar to that of nitrate ( $r = 0.53$ ), corroborating its  
541 semi-volatile feature. Different from other factors, LV-OOA concentrations increase  
542 during daytime and shows positive correlation with temperature ( $r = 0.76$ ); it also has  
543 negative correlation with the diurnal cycle of RH ( $r = -0.75$ ). Both behaviors are  
544 similar to those of sulfate ( $r = 0.72$  for the diurnal cycle of LV-OOA vs. sulfate),  
545 indicating the leading role of photochemical oxidation for LV-OOA formation as well.

546 As shown in Fig. 10b, due to mainly the increase of LV-OOA mass loading, OA is  
547 overwhelmingly dominated by the SOA (SV-OOA + LV-OOA) during afternoon (80.2%  
548 at 3 pm); POA (HOA + COA) only dominates the OA mass during morning (53.2% at  
549 7 am) and early evening (56.9% at 8 pm) in response to the enhanced traffic and  
550 cooking emissions. On average, the OA is composed of 27.6% of HOA, 16.9% of

551 COA, 27.4% of SV-OOA and 28.1% of LV-OOA (Fig. 10c), with SOA outweighing  
552 POA (55.5% vs. 44.5%). However, as shown in Fig. 10d, with the increase of OA  
553 mass loadings, the fractional contribution of POA increases, highlighting the  
554 important and direct influences of anthropogenic emissions on the heavy pollution  
555 haze events.

556

### 557 **3.5.3 Local/regional influences and evolution processes of the OA factors**

558 Combining WS, WD and mass loadings, the bivariate polar plots of the four OA  
559 factors,  $\tau$ BC, total OA, nitrate, sulfate and the total PM<sub>1</sub> are shown in Fig. 11. These  
560 plots provide an effective graphical method for showing the potential influences of air  
561 masses from different directions with different wind speeds to the receptor site  
562 (Carslaw and Beevers, 2013). Clearly, high mass loadings of HOA and  $\tau$ BC mostly  
563 link with low WS ( $< 1 \text{ m s}^{-1}$ ), indicating they are mainly from local vehicle emissions.  
564 High COA concentrations occur mainly under low WS as well, but with some high  
565 concentrations accompanied with air masses from southeast under higher WS.  
566 SV-OOA appears to be mainly formed locally, except for a concentration hotspot in  
567 the southeast – likely due to emissions from the tobacco factory that resides in that  
568 direction. Nitrate, as a semi-volatile species, behaves overall similar to the SV-OOA.  
569 High concentrations of LV-OOA are distributed in all directions under higher WS,  
570 similar to that of sulfate, representing their regional behaviors. Overall, high PM<sub>1</sub>  
571 mass loadings occur mainly under low WS, indicating that the PM<sub>1</sub> is heavily affected  
572 by local emissions rather than pollutants in a regional scale.

573 The aging of OA can be described in general by the increase of O/C and decrease  
574 of H/C. In this regard, we plotted the Van Krevelen diagram (Heald et al., 2010) (Fig.  
575 12a) to show the relationships between H/C and O/C ratios for all OA as well as the  
576 four OA factors. Overall, in this study, the H/C and O/C ratios of OA data are  
577 correlated linearly with a slope of -1.04 ( $r^2 = 0.93$ ). Interestingly, the two OOA factors  
578 lie very well on the fitted straight line. This trend may suggest that the evolution of  
579 secondary OA during this campaign follows a transformation pathway of SV-OOA to

580 LV-OOA. The diurnal cycle of LV-OOA varies oppositely to that of SV-OOA ( $r =$   
581  $-0.86$ ), probably supporting this hypothesis. In addition, SV-OOA and LV-OOA mass  
582 concentrations, and O/C ratios of OA all show no obvious correlations with the RH as  
583 shown in Fig. 12b and Fig. 12c, indicating that aqueous-phase processing is  
584 insignificant compared to the photochemical processing for the oxidation of OA.

585

#### 586 **4. Conclusions**

587 We present for the first time the real-time measurement results using the SP-AMS  
588 on submicron aerosols in urban Nanjing during springtime (April 13 - 29, 2015). The  
589 dynamic variations of SP-AMS determined  $PM_{10}$  mass loadings, agreed well with the  
590  $PM_{2.5}$  measured by the Met One  $PM_{2.5}$  analyzer. The average  $PM_{10}$  concentration was  
591  $28.2 \mu\text{g m}^{-3}$ , lower than previously ACSM-determined  $PM_{10}$  concentrations during  
592 summer and winter in Nanjing. Organics on average comprised the largest fraction  
593 (45%) of  $PM_{10}$ , and its fractional contributions increased in case of high  $PM_{10}$  mass  
594 loadings. The diurnal cycles of mass concentrations of organics,  $rBC$ , nitrate and  
595 chloride all presented a similar behavior, which was high in early morning and  
596 evening, but low in the afternoon. Concentrations of sulfate, on the contrary, increased  
597 during afternoon. Further investigations of  $f_s$ , sulfate concentrations and its  
598 relationship with RH suggest that photochemical processing contributed significantly  
599 to sulfate formation compared to the aqueous-phase processing, while nitrate (and  
600 chloride) formation was mainly governed by the thermodynamic equilibrium. The  
601 chemically-resolved mass-based size distribution data showed that  $rBC$  occupied a  
602 large fraction of ultrafine particles, while secondary inorganic species could dominate  
603 the mass of particles larger than 400 nm ( $D_{va}$ ). In addition, by using the IMPROVE  
604 method, we found that the observed  $PM_{10}$  components were able to reproduce  $\sim 44\%$   
605 of the light extinction during this study.

606 PMF analyses resolved four OA factors, e.g., HOA, COA, SV-OOA and LV-OOA.  
607 Mass spectral profiles of these factors agree very well with the corresponding factors  
608 identified at other locations. The springtime OA showed no influences from biomass

609 burning emissions. On average, the OA is dominated by SOA (55.5%), but POA  
610 appeared to be more important when the OA mass loadings are high, and can be  
611 dominant in early morning and evening. Diurnal cycle of SV-OOA varied similarly to  
612 that of nitrate, reflecting its semi-volatile behavior. Diurnal variations of LV-OOA  
613 showed great resemblance to that of sulfate. The bivariate polar plots indicate that  
614 SV-OOA was formed locally, and the Van Krevelen diagram further suggests a  
615 transformation from SV-OOA to LV-OOA in Nanjing. Generally, our highly  
616 time-resolved SP-AMS measurement results may offer useful insights into the aerosol  
617 chemistry, and have important implications for the PM control and reduction in this  
618 densely populated region.

619

#### 620 **Acknowledgements**

621 This work was supported by the Natural Science Foundation of China (Grant Nos.  
622 21407079 and 91544220), the Jiangsu Natural Science Foundation (BK20150042),  
623 the Jiangsu Provincial Specially-Appointed Professors Foundation, the LAPC Open  
624 Fund (LAPC-KF-2014-06), and the project funded by the Priority Academic Program  
625 Development of Jiangsu Higher Education Institutions (PAPD). M. Chen  
626 acknowledges the support from the Natural Science Foundation of China (Grant Nos.  
627 21577065 and 91543115), the Commonwealth Program of Environment Protection  
628 Department of China (201409027-05), and the International ST Cooperation Program  
629 of China (2014DFA90780). J. Wang also acknowledges the financial support from  
630 China Scholarship Council, and the innovative project for graduate student of Jiangsu  
631 Province. The authors thank Nanjing Environmental Monitoring Center for the  
632 supporting data, and the helps from Ling Li, Yanan He, Hui Chen and Yangzhou Wu  
633 during the campaign and preparation of the manuscript.

634

635 References

- 636 Aiken, A. C., Decarlo, P. F., Kroll, J. H., Worsnop, D. R., Huffman, J. A., Docherty, K. S.,  
637 Ulbrich, I. M., Mohr, C., Kimmel, J. R., Sueper, D., Sun, Y., Zhang, Q., Trimborn, A.,  
638 Northway, M., Ziemann, P. J., Canagaratna, M. R., Onasch, T. B., Alfarra, M. R., Prevot, A. S.  
639 H., Dommen, J., Duplissy, J., Metzger, A., Baltensperger, U., and Jimenez, J. L.: O/C and  
640 OM/OC ratios of primary, secondary, and ambient organic aerosols with high-resolution  
641 time-of-flight aerosol mass spectrometry, *Environ. Sci. Technol.*, 42, 4478-4485,  
642 10.1021/Es703009q, 2008.
- 643 Alfarra, M. R., Prevot, A. S. H., Szidat, S., Sandradewi, J., Weimer, S., Lanz, V. A., Schreiber,  
644 D., Mohr, M., and Baltensperger, U.: Identification of the Mass Spectral Signature of Organic  
645 Aerosols from Wood Burning Emissions, *Environ. Sci. Technol.*, 41, 5770-5777,  
646 10.1021/es062289b, 2007.
- 647 Allan, J. D., Williams, P. I., Morgan, W. T., Martin, C. L., Flynn, M. J., Lee, J., Nemitz, E.,  
648 Phillips, G. J., Gallagher, M. W., and Coe, H.: Contributions from transport, solid fuel burning  
649 and cooking to primary organic aerosols in two UK cities, *Atmos. Chem. Phys.*, 10, 647-668,  
650 10.5194/acp-10-647-2010, 2010.
- 651 Canagaratna, M. R., Jayne, J. T., Ghertner, D. A., Herndon, S., Shi, Q., Jimenez, J. L., Silva, P.  
652 J., Williams, P., Lanni, T., Drewnick, F., Demerjian, K. L., Kolb, C. E., and Worsnop, D. R.:  
653 Chase studies of particulate emissions from in-use New York City vehicles, *Aerosol Sci. Tech.*,  
654 38, 555-573, 10.1080/02786820490465504, 2004.
- 655 Canagaratna, M. R., Jayne, J. T., Jimenez, J. L., Allan, J. D., Alfarra, M. R., Zhang, Q.,  
656 Onasch, T. B., Drewnick, F., Coe, H., Middlebrook, A., Delia, A., Williams, L. R., Trimborn,  
657 A. M., Northway, M. J., DeCarlo, P. F., Kolb, C. E., Davidovits, P., and Worsnop, D. R.:  
658 Chemical and microphysical characterization of ambient aerosols with the aerodyne aerosol  
659 mass spectrometer, *Mass Spectrom. Rev.*, 26, 185-222, 10.1002/Mas.20115, 2007.
- 660 Canagaratna, M. R., Jimenez, J. L., Kroll, J. H., Chen, Q., Kessler, S. H., Massoli, P.,  
661 Hildebrandt Ruiz, L., Fortner, E., Williams, L. R., Wilson, K. R., Surratt, J. D., Donahue, N.  
662 M., Jayne, J. T., and Worsnop, D. R.: Elemental ratio measurements of organic compounds  
663 using aerosol mass spectrometry: characterization, improved calibration, and implications,  
664 *Atmos. Chem. Phys.*, 15, 253-272, 10.5194/acp-15-253-2015, 2015.
- 665 Cao, J. J., Xu, H. M., Xu, Q., Chen, B. H., and Kan, H. D.: Fine Particulate Matter  
666 Constituents and Cardiopulmonary Mortality in a Heavily Polluted Chinese City, *Environ.*  
667 *Health Persp.*, 120, 373-378, 10.1289/ehp.1103671, 2012.
- 668 Carslaw, D. C., and Beevers, S. D.: Characterising and understanding emission sources using  
669 bivariate polar plots and k-means clustering, *Environ. Model. Soft.*, 40, 325-329,  
670 10.1016/j.envsoft.2012.09.005, 2013.
- 671 Carslaw, K. S., Boucher, O., Spracklen, D. V., Mann, G. W., Rae, J. G. L., Woodward, S., and

672 Kulmala, M.: A review of natural aerosol interactions and feedbacks within the Earth system,  
673 *Atmos. Chem. Phys.*, 10, 1701-1737, 10.5194/acp-10-1701-2010, 2010.

674 Chen, C., Sun, Y. L., Xu, W. Q., Du, W., Zhou, L. B., Han, T. T., Wang, Q. Q., Fu, P. Q., Wang,  
675 Z. F., Gao, Z. Q., Zhang, Q., and Worsnop, D. R.: Characteristics and sources of submicron  
676 aerosols above the urban canopy (260 m) in Beijing, China, during the 2014 APEC summit,  
677 *Atmos. Chem. Phys.*, 15, 12879-12895, 10.5194/acp-15-12879-2015, 2015.

678 Collier, S., Zhou, S., Kuwayama, T., Forestieri, S., Brady, J., Zhang, M., Kleeman, M., Cappa,  
679 C., Bertram, T., and Zhang, Q.: Organic PM Emissions from Vehicles: Composition, O/C  
680 Ratio, and Dependence on PM Concentration, *Aerosol Sci. Tech.*, 49, 86-97,  
681 10.1080/02786826.2014.1003364, 2015.

682 DeCarlo, P. F., Slowik, J. G., Worsnop, D. R., Davidovits, P., and Jimenez, J. L.: Particle  
683 morphology and density characterization by combined mobility and aerodynamic diameter  
684 measurements. Part 1: Theory, *Aerosol Sci. Tech.*, 38, 1185-1205,  
685 10.1080/02786820590928897, 2004.

686 DeCarlo, P. F., Kimmel, J. R., Trimborn, A., Northway, M. J., Jayne, J. T., Aiken, A. C., Gonin,  
687 M., Fuhrer, K., Horvath, T., Docherty, K. S., Worsnop, D. R., and Jimenez, J. L.:  
688 Field-deployable, high-resolution, time-of-flight aerosol mass spectrometer, *Anal. Chem.*, 78,  
689 8281-8289, 10.1021/Ac061249n, 2006.

690 Denjean, C., Formenti, P., Picquet-Varrault, B., Pangui, E., Zapf, P., Katrib, Y., Giorio, C.,  
691 Tapparo, A., Monod, A., Temime-Roussel, B., Decorse, P., Mangeney, C., and Doussin, J. F.:  
692 Relating hygroscopicity and optical properties to chemical composition and structure of  
693 secondary organic aerosol particles generated from the ozonolysis of  $\alpha$ -pinene, *Atmos. Chem.*  
694 *Phys.*, 15, 3339-3358, 10.5194/acp-15-3339-2015, 2015.

695 Dong, H. B., Zeng, L. M., Hu, M., Wu, Y. S., Zhang, Y. H., Slanina, J., Zheng, M., Wang, Z.  
696 F., and Jansen, R.: Technical Note: The application of an improved gas and aerosol collector  
697 for ambient air pollutants in China, *Atmos. Chem. Phys.*, 12, 10519-10533,  
698 10.5194/acp-12-10519-2012, 2012.

699 Drewnick, F., Hings, S. S., DeCarlo, P., Jayne, J. T., Gonin, M., Fuhrer, K., Weimer, S.,  
700 Jimenez, J. L., Demerjian, K. L., Borrmann, S., and Worsnop, D. R.: A new time-of-flight  
701 aerosol mass spectrometer (TOF-AMS) - Instrument description and first field deployment,  
702 *Aerosol Sci. Tech.*, 39, 637-658, 10.1080/02786820500182040, 2005.

703 Du, W., Sun, Y. L., Xu, Y. S., Jiang, Q., Wang, Q. Q., Yang, W., Wang, F., Bai, Z. P., Zhao, X.  
704 D., and Yang, Y. C.: Chemical characterization of submicron aerosol and particle growth  
705 events at a national background site (3295 m a.s.l.) on the Tibetan Plateau, *Atmos. Chem.*  
706 *Phys.*, 15, 10811-10824, 10.5194/acp-15-10811-2015, 2015.

707 Duplissy, J., DeCarlo, P. F., Dommen, J., Alfarra, M. R., Metzger, A., Barmpadimos, I., Prevot,  
708 A. S. H., Weingartner, E., Tritscher, T., Gysel, M., Aiken, A. C., Jimenez, J. L., Canagaratna,



709 M. R., Worsnop, D. R., Collins, D. R., Tomlinson, J., and Baltensperger, U.: Relating  
710 hygroscopicity and composition of organic aerosol particulate matter, *Atmos. Chem. Phys.*, 11,  
711 1155-1165, 10.5194/acp-11-1155-2011, 2011.

712 Fröhlich, R., Cubison, M. J., Slowik, J. G., Bukowiecki, N., Prévôt, A. S. H., Baltensperger,  
713 U., Schneider, J., Kimmel, J. R., Gonin, M., Rohner, U., Worsnop, D. R., and Jayne, J. T.: The  
714 ToF-ACSM: a portable aerosol chemical speciation monitor with TOFMS detection, *Atmos.*  
715 *Meas. Tech.*, 6, 3225-3241, 10.5194/amt-6-3225-2013, 2013.

716 Fu, Q. Y., Zhuang, G. S., Wang, J., Xu, C., Huang, K., Li, J., Hou, B., Lu, T., and Streets, D.  
717 G.: Mechanism of formation of the heaviest pollution episode ever recorded in the Yangtze  
718 River Delta, China, *Atmos. Environ.*, 42, 2023-2036, 10.1016/j.atmosenv.2007.12.002, 2008.

719 Ge, X., Zhang, Q., Sun, Y., Ruehl, C. R., and Setyan, A.: Effect of aqueous-phase processing  
720 on aerosol chemistry and size distributions in Fresno, California, during wintertime, *Environ.*  
721 *Chem.*, 9, 221-235, 10.1071/EN11168, 2012a.

722 Ge, X. L., Setyan, A., Sun, Y., and Zhang, Q.: Primary and secondary organic aerosols in  
723 Fresno, California during wintertime: Results from high resolution aerosol mass spectrometry,  
724 *J. Geophys. Res. - Atmos.*, 117, D19301, 10.1029/2012jd018026, 2012b.

725 Ghan, S. J., and Schwartz, S. E.: Aerosol properties and processes: A path from field and  
726 laboratory measurements to global climate models, *Bull. Am. Meteorol. Soc.*, 88, 1059-1083,  
727 10.1175/bams-88-7-1059, 2007.

728 Han, T., Xu, W., Chen, C., Liu, X., Wang, Q., Li, J., Zhao, X., Du, W., Wang, Z., and Sun, Y.:  
729 Chemical apportionment of aerosol optical properties during the Asia-Pacific Economic  
730 Cooperation summit in Beijing, China, *J. Geophys. Res. - Atmos.*, 120, 212,281-212,295,  
731 10.1002/2015JD023918, 2015.

732 He, L. Y., Huang, X.-F., Xue, L., Hu, M., Lin, Y., Zheng, J., Zhang, R., and Zhang, Y.-H.:  
733 Submicron aerosol analysis and organic source apportionment in an urban atmosphere in  
734 Pearl River Delta of China using high-resolution aerosol mass spectrometry, *J. Geophys. Res.*  
735 *- Atmos.*, 116, D12304, 10.1029/2010jd014566, 2011.

736 Heald, C. L., Kroll, J. H., Jimenez, J. L., Docherty, K. S., DeCarlo, P. F., Aiken, A. C., Chen,  
737 Q., Martin, S. T., Farmer, D. K., and Artaxo, P.: A simplified description of the evolution of  
738 organic aerosol composition in the atmosphere, *Geophys. Res. Lett.*, 37, L08803,  
739 10.1029/2010gl042737, 2010.

740 Hu, J., Ying, Q., Wang, Y., and Zhang, H.: Characterizing multi-pollutant air pollution in  
741 China: Comparison of three air quality indices, *Environ. Int.*, 84, 17-25,  
742 10.1016/j.envint.2015.06.014, 2015.

743 Hu, W. W., Hu, M., Yuan, B., Jimenez, J. L., Tang, Q., Peng, J. F., Hu, W., Shao, M., Wang,  
744 M., Zeng, L. M., Wu, Y. S., Gong, Z. H., Huang, X. F., and He, L. Y.: Insights on organic

745 aerosol aging and the influence of coal combustion at a regional receptor site of central  
746 eastern China, *Atmos. Chem. Phys.*, 13, 10095-10112, 10.5194/acp-13-10095-2013, 2013.

747 Hu, X., Zhang, Y., Ding, Z. H., Wang, T. J., Lian, H. Z., Sun, Y. Y., and Wu, J. C.:  
748 Bioaccessibility and health risk of arsenic and heavy metals (Cd, Co, Cr, Cu, Ni, Pb, Zn and  
749 Mn) in TSP and PM<sub>2.5</sub> in Nanjing, China, *Atmos. Environ.*, 57, 146-152,  
750 10.1016/j.atmosenv.2012.04.056, 2012.

751 Huang, X., Xue, L., Tian, X.-D., Shao, W.-W., Sun, T.-L., Gong, Z.-H., Ju, W.-W., Jiang, B.,  
752 Hu, M., and He, L.-Y.: Highly time-resolved carbonaceous aerosol characterization in Yangtze  
753 River Delta of China: composition, mixing state and secondary formation, *Atmos. Environ.*,  
754 10.1016/j.atmosenv.2012.09.059, 2012a.

755 Huang, X. F., He, L. Y., Hu, M., Canagaratna, M. R., Sun, Y., Zhang, Q., Zhu, T., Xue, L.,  
756 Zeng, L. W., Liu, X. G., Zhang, Y. H., Jayne, J. T., Ng, N. L., and Worsnop, D. R.: Highly  
757 time-resolved chemical characterization of atmospheric submicron particles during 2008  
758 Beijing Olympic Games using an Aerodyne High-Resolution Aerosol Mass Spectrometer,  
759 *Atmos. Chem. Phys.*, 10, 8933-8945, 10.5194/acp-10-8933-2010, 2010.

760 Huang, X. F., He, L. Y., Hu, M., Canagaratna, M. R., Kroll, J. H., Ng, N. L., Zhang, Y. H., Lin,  
761 Y., Xue, L., Sun, T. L., Liu, X. G., Shao, M., Jayne, J. T., and Worsnop, D. R.:  
762 Characterization of submicron aerosols at a rural site in Pearl River Delta of China using an  
763 Aerodyne High-Resolution Aerosol Mass Spectrometer, *Atmos. Chem. Phys.*, 11, 1865-1877,  
764 10.5194/acp-11-1865-2011, 2011.

765 Huang, X. F., He, L. Y., Xue, L., Sun, T. L., Zeng, L. W., Gong, Z. H., Hu, M., and Zhu, T.:  
766 Highly time-resolved chemical characterization of atmospheric fine particles during 2010  
767 Shanghai World Expo, *Atmos. Chem. Phys.*, 12, 4897-4907, 10.5194/acp-12-4897-2012,  
768 2012b.

769 Jayne, J. T., Leard, D. C., Zhang, X., Davidovits, P., Smith, K. A., Kolb, C. E., and Worsnop,  
770 D. R.: Development of an Aerosol Mass Spectrometer for Size and Composition Analysis of  
771 Submicron Particles, *Aerosol Sci. Tech.*, 33, 49 - 70, 10.1016/S0021-8502(98)00158-X, 2000.

772 Jiang, Q., Sun, Y. L., Wang, Z., and Yin, Y.: Aerosol composition and sources during the  
773 Chinese Spring Festival: fireworks, secondary aerosol, and holiday effects, *Atmos. Chem.*  
774 *Phys.*, 15, 6023-6034, 10.5194/acp-15-6023-2015, 2015.

775 Jimenez, J. L., Jayne, J. T., Shi, Q., Kolb, C. E., Worsnop, D. R., Yourshaw, I., Seinfeld, J. H.,  
776 Flagan, R. C., Zhang, X. F., Smith, K. A., Morris, J. W., and Davidovits, P.: Ambient aerosol  
777 sampling using the Aerodyne Aerosol Mass Spectrometer, *J. Geophys. Res. - Atmos.*, 108,  
778 8425, 10.1029/2001jd001213, 2003.

779 Jimenez, J. L., Canagaratna, M. R., Donahue, N. M., Prevot, A. S. H., Zhang, Q., Kroll, J. H.,  
780 DeCarlo, P. F., Allan, J. D., Coe, H., Ng, N. L., Aiken, A. C., Docherty, K. S., Ulbrich, I. M.,  
781 Grieshop, A. P., Robinson, A. L., Duplissy, J., Smith, J. D., Wilson, K. R., Lanz, V. A.,

782 Hueglin, C., Sun, Y. L., Tian, J., Laaksonen, A., Raatikainen, T., Rautiainen, J., Vaattovaara, P.,  
783 Ehn, M., Kulmala, M., Tomlinson, J. M., Collins, D. R., Cubison, M. J., Dunlea, E. J.,  
784 Huffman, J. A., Onasch, T. B., Alfarra, M. R., Williams, P. I., Bower, K., Kondo, Y., Schneider,  
785 J., Drewnick, F., Borrmann, S., Weimer, S., Demerjian, K., Salcedo, D., Cottrell, L., Griffin,  
786 R., Takami, A., Miyoshi, T., Hatakeyama, S., Shimono, A., Sun, J. Y., Zhang, Y. M., Dzepina,  
787 K., Kimmel, J. R., Sueper, D., Jayne, J. T., Herndon, S. C., Trimborn, A. M., Williams, L. R.,  
788 Wood, E. C., Middlebrook, A. M., Kolb, C. E., Baltensperger, U., and Worsnop, D. R.:  
789 Evolution of organic aerosols in the atmosphere, *Science*, 326, 1525-1529,  
790 10.1126/science.1180353, 2009.

791 Kong, S. F., Li, L., Li, X. X., Yin, Y., Chen, K., Liu, D. T., Yuan, L., Zhang, Y. J., Shan, Y. P.,  
792 and Ji, Y. Q.: The impacts of firework burning at the Chinese Spring Festival on air quality:  
793 insights of tracers, source evolution and aging processes, *Atmos. Chem. Phys.*, 15, 2167-2184,  
794 10.5194/acp-15-2167-2015, 2015.

795 Kulmala, M., Lappalainen, H. K., Petäjä, T., Kurten, T., Kerminen, V. M., Viisanen, Y., Hari,  
796 P., Sorvari, S., Bäck, J., Bondur, V., Kasimov, N., Kotlyakov, V., Matvienko, G., Baklanov, A.,  
797 Guo, H. D., Ding, A., Hansson, H. C., and Zilitinkevich, S.: Introduction: The Pan-Eurasian  
798 Experiment (PEEX) – multidisciplinary, multiscale and multicomponent research and  
799 capacity-building initiative, *Atmos. Chem. Phys.*, 15, 13085-13096,  
800 10.5194/acp-15-13085-2015, 2015.

801 Lee, A. K. Y., Hayden, K. L., Herckes, P., Leaitch, W. R., Liggio, J., Macdonald, A. M., and  
802 Abbatt, J. P. D.: Characterization of aerosol and cloud water at a mountain site during WACS  
803 2010: secondary organic aerosol formation through oxidative cloud processing, *Atmos. Chem.*  
804 *Phys.*, 12, 7103-7116, 10.5194/acp-12-7103-2012, 2012.

805 Lee, B. P., Li, Y. J., Yu, J. Z., Louie, P. K. K., and Chan, C. K.: Physical and chemical  
806 characterization of ambient aerosol by HR-ToF-AMS at a suburban site in Hong Kong during  
807 springtime 2011, *J. Geophys. Res. - Atmos.*, 118, 8625-8639, 10.1002/jgrd.50658, 2013.

808 Li, Y. J., Lee, B. P., Su, L., Fung, J. C. H., and Chan, C. K.: Seasonal characteristics of fine  
809 particulate matter (PM) based on high-resolution time-of-flight aerosol mass spectrometric  
810 (HR-ToF-AMS) measurements at the HKUST Supersite in Hong Kong, *Atmos. Chem. Phys.*,  
811 15, 37-53, 10.5194/acp-15-37-2015, 2015.

812 Malm, W. C., and Day, D. E.: Estimates of aerosol species scattering characteristics as a  
813 function of relative humidity, *Atmos. Environ.*, 35, 2845-2860,  
814 10.1016/S1352-2310(01)00077-2, 2001.

815 Matthew, B. M., Middlebrook, A. M., and Onasch, T. B.: Collection Efficiencies in an  
816 Aerodyne Aerosol Mass Spectrometer as a Function of Particle Phase for Laboratory  
817 Generated Aerosols, *Aerosol Sci. Tech.*, 42, 884-898, 10.1080/02786820802356797, 2008.

818 Middlebrook, A. M., Bahreini, R., Jimenez, J. L., and Canagaratna, M. R.: Evaluation of  
819 Composition-Dependent Collection Efficiencies for the Aerodyne Aerosol Mass Spectrometer

820 using Field Data, *Aerosol Sci. Tech.*, 46, 258-271, 10.1080/02786826.2011.620041, 2012.

821 Mohr, C., DeCarlo, P. F., Heringa, M. F., Chirico, R., Slowik, J. G., Richter, R., Reche, C.,  
822 Alastuey, A., Querol, X., Seco, R., Peñuelas, J., Jiménez, J. L., Crippa, M., Zimmermann, R.,  
823 Baltensperger, U., and Prévôt, A. S. H.: Identification and quantification of organic aerosol  
824 from cooking and other sources in Barcelona using aerosol mass spectrometer data, *Atmos.*  
825 *Chem. Phys.*, 12, 1649-1665, 10.5194/acp-12-1649-2012, 2012.

826 Mohr, C., DeCarlo, P. F., Heringa, M. F., Chirico, R., Richter, R., Crippa, M., Querol, X.,  
827 Baltensperger, U., and Prévôt, A. S. H.: Spatial Variation of Aerosol Chemical Composition  
828 and Organic Components Identified by Positive Matrix Factorization in the Barcelona Region,  
829 *Environ. Sci. Technol.*, 49, 10421-10430, 10.1021/acs.est.5b02149, 2015.

830 Ng, N. L., Canagaratna, M. R., Zhang, Q., Jimenez, J. L., Tian, J., Ulbrich, I. M., Kroll, J. H.,  
831 Docherty, K. S., Chhabra, P. S., Bahreini, R., Murphy, S. M., Seinfeld, J. H., Hildebrandt, L.,  
832 Donahue, N. M., DeCarlo, P. F., Lanz, V. A., Prevot, A. S. H., Dinar, E., Rudich, Y., and  
833 Worsnop, D. R.: Organic aerosol components observed in Northern Hemispheric datasets  
834 from Aerosol Mass Spectrometry, *Atmos. Chem. Phys.*, 10, 4625-4641,  
835 10.5194/acp-10-4625-2010, 2010.

836 Ng, N. L., Herndon, S. C., Trimborn, A., Canagaratna, M. R., Croteau, P. L., Onasch, T. B.,  
837 Sueper, D., Worsnop, D. R., Zhang, Q., Sun, Y. L., and Jayne, J. T.: An Aerosol Chemical  
838 Speciation Monitor (ACSM) for Routine Monitoring of the Composition and Mass  
839 Concentrations of Ambient Aerosol, *Aerosol Sci. Tech.*, 45, 770-784,  
840 10.1080/02786826.2011.560211, 2011.

841 Onasch, T. B., Trimborn, A., Fortner, E. C., Jayne, J. T., Kok, G. L., Williams, L. R.,  
842 Davidovits, P., and Worsnop, D. R.: Soot particle aerosol mass spectrometer: Development,  
843 validation, and initial application, *Aerosol Sci. Tech.*, 46, 804-817,  
844 10.1080/02786826.2012.663948, 2012.

845 Onasch, T. B., Fortner, E. C., Trimborn, A. M., Lambe, A. T., Tiwari, A. J., Marr, L. C.,  
846 Corbin, J. C., Mensah, A. A., Williams, L. R., Davidovits, P., and Worsnop, D. R.:  
847 Investigations of SP-AMS Carbon Ion Distributions as a Function of Refractory Black  
848 Carbon Particle Type, *Aerosol Sci. Tech.*, 49, 409-422, 10.1080/02786826.2015.1039959,  
849 2015.

850 Paatero, P., and Tapper, U.: Positive matrix factorization: A non-negative factor model with  
851 optimal utilization of error estimates of data values, *Environmetrics*, 5, 111-126,  
852 10.1002/env.3170050203, 1994.

853 Pope, C. A., and Dockery, D. W.: Health Effects of Fine Particulate Air Pollution: Lines that  
854 Connect, *J. Air Waste Manage.*, 56, 709-742, 10.1080/10473289.2006.10464485, 2006.

855 Pöschl, U.: Atmospheric Aerosols: Composition, Transformation, Climate and Health Effects,  
856 *Angewandte Chemie International Edition*, 44, 7520-7540, 10.1002/anie.200501122, 2005.

857 Qi, L., Zhang, Y., Ma, Y., Chen, M., Ge, X., Ma, Y., Zheng, J., Wang, Z., and Li, S.: Source  
858 identification of trace elements in the atmosphere during the second Asian Youth Games in  
859 Nanjing, China: Influence of control measures on air quality, *Atmos. Pollut. Res.*, 7, 547-556,  
860 <http://dx.doi.org/10.1016/j.apr.2016.01.003>, 2016.

861 Seinfeld, J. H., and Pandis, S. N.: *Atmospheric Chemistry and Physics: From Air Pollution to*  
862 *Climate Change*, John Wiley & Sons, New York, 2006.

863 Setyan, A., Zhang, Q., Merkel, M., Knighton, W. B., Sun, Y., Song, C., Shilling, J. E., Onasch,  
864 T. B., Herndon, S. C., Worsnop, D. R., Fast, J. D., Zaveri, R. A., Berg, L. K., Wiedensohler, A.,  
865 Flowers, B. A., Dubey, M. K., and Subramanian, R.: Characterization of submicron particles  
866 influenced by mixed biogenic and anthropogenic emissions using high-resolution aerosol  
867 mass spectrometry: results from CARES, *Atmos. Chem. Phys.*, 12, 8131-8156,  
868 [10.5194/acp-12-8131-2012](https://doi.org/10.5194/acp-12-8131-2012), 2012.

869 Shen, G. F., Yuan, S. Y., Xie, Y. N., Xia, S. J., Li, L., Yao, Y. K., Qiao, Y. Z., Zhang, J., Zhao,  
870 Q. Y., Ding, A. J., Li, B., and Wu, H. S.: Ambient levels and temporal variations of PM<sub>2.5</sub> and  
871 PM<sub>10</sub> at a residential site in the mega-city, Nanjing, in the western Yangtze River Delta, China,  
872 *J. Environ. Sci. Health., Part A*, 49, 171-178, [10.1080/10934529.2013.838851](https://doi.org/10.1080/10934529.2013.838851), 2014.

873 Shen, X. J., Sun, J. Y., Zhang, X. Y., Zhang, Y. M., Zhang, L., Che, H. C., Ma, Q. L., Yu, X.  
874 M., Yue, Y., and Zhang, Y. W.: Characterization of submicron aerosols and effect on visibility  
875 during a severe haze-fog episode in Yangtze River Delta, China, *Atmos. Environ.*, 120,  
876 307-316, [10.1016/j.atmosenv.2015.09.011](https://doi.org/10.1016/j.atmosenv.2015.09.011), 2015.

877 Sun, Y., Jiang, Q., Wang, Z., Fu, P., Li, J., Yang, T., and Yin, Y.: Investigation of the Sources  
878 and Evolution Processes of Severe Haze Pollution in Beijing in January 2013, *J. Geophys.*  
879 *Res. - Atmos.*, 2014JD021641, [10.1002/2014JD021641](https://doi.org/10.1002/2014JD021641), 2014.

880 Sun, Y. L., Zhang, Q., Schwab, J. J., Demerjian, K. L., Chen, W. N., Bae, M. S., Hung, H. M.,  
881 Hogrefe, O., Frank, B., Rattigan, O. V., and Lin, Y. C.: Characterization of the sources and  
882 processes of organic and inorganic aerosols in New York city with a high-resolution  
883 time-of-flight aerosol mass spectrometer, *Atmos. Chem. Phys.*, 11, 1581-1602,  
884 [10.5194/acp-11-1581-2011](https://doi.org/10.5194/acp-11-1581-2011), 2011.

885 Sun, Y. L., Du, W., Wang, Q., Zhang, Q., Chen, C., Chen, Y., Chen, Z., Fu, P., Wang, Z., Gao,  
886 Z., and Worsnop, D. R.: Real-Time Characterization of Aerosol Particle Composition above  
887 the Urban Canopy in Beijing: Insights into the Interactions between the Atmospheric  
888 Boundary Layer and Aerosol Chemistry, *Environ. Sci. Technol.*, 49, 11340-11347,  
889 [10.1021/acs.est.5b02373](https://doi.org/10.1021/acs.est.5b02373), 2015a.

890 Sun, Y. L., Wang, Z. F., Du, W., Zhang, Q., Wang, Q. Q., Fu, P. Q., Pan, X. L., Li, J., Jayne, J.,  
891 and Worsnop, D. R.: Long-term real-time measurements of aerosol particle composition in  
892 Beijing, China: seasonal variations, meteorological effects, and source analysis, *Atmos. Chem.*  
893 *Phys.*, 15, 10149-10165, [10.5194/acp-15-10149-2015](https://doi.org/10.5194/acp-15-10149-2015), 2015b.

894 Sun, Y. L., Wang, Z., Wild, O., Xu, W., Chen, C., Fu, P., Du, W., Zhou, L., Zhang, Q., Han, T.,  
895 Wang, Q., Pan, X., Zheng, H., Li, J., Guo, X., Liu, J., and Worsnop, D. R.: “APEC Blue”:  
896 Secondary Aerosol Reductions from Emission Controls in Beijing, *Sci. Rep.*, 6, 20668,  
897 10.1038/srep20668, 2016.

898 Tang, L., Yu, H., Ding, A., Zhang, Y., Qin, W., Wang, Z., Chen, W., Hua, Y., and Yang, X.:  
899 Regional contribution to PM<sub>1</sub> pollution during winter haze in Yangtze River Delta, China, *Sci.*  
900 *Total Environ.*, 541, 161-166, 10.1016/j.scitotenv.2015.05.058, 2016.

901 Ulbrich, I. M., Canagaratna, M. R., Zhang, Q., Worsnop, D. R., and Jimenez, J. L.:  
902 Interpretation of organic components from Positive Matrix Factorization of aerosol mass  
903 spectrometric data, *Atmos. Chem. Phys.*, 9, 2891-2918, 10.5194/acp-9-2891-2009, 2009.

904 Wang, G. H., Niu, S. L., Liu, C., and Wang, L. S.: Identification of dicarboxylic acids and  
905 aldehyde of PM<sub>10</sub> and PM<sub>2.5</sub> aerosols in Nanjing, China, *Atmos. Environ.*, 36, 1941-1950,  
906 10.1016/s1352-2310(02)00180-2, 2002.

907 Wang, G. H., Wang, H., Yu, Y. J., Gao, S. X., Feng, J. F., Gao, S. T., and Wang, L. S.:  
908 Chemical characterization of water-soluble components of PM<sub>10</sub> and PM<sub>2.5</sub> atmospheric  
909 aerosols in five locations of Nanjing, China, *Atmos. Environ.*, 37, 2893-2902,  
910 10.1016/s1352-2310(03)00271-1, 2003.

911 Wang, G. H., Kawamura, K., Xie, M. J., Hu, S. Y., Cao, J. J., An, Z. S., Weston, J. G., and  
912 Chow, J. C.: Organic molecular compositions and size distributions of Chinese summer and  
913 autumn aerosols from Nanjing: Characteristic haze event caused by wheat straw burning,  
914 *Environ. Sci. Technol.*, 43, 6493-6499, 10.1021/es803086g, 2009.

915 Wang, G. H., Chen, C. L., Li, J. J., Zhou, B. H., Xie, M. J., Hu, S. Y., Kawamura, K., and  
916 Chen, Y.: Molecular composition and size distribution of sugars, sugar-alcohols and  
917 carboxylic acids in airborne particles during a severe urban haze event caused by wheat straw  
918 burning, *Atmos. Environ.*, 45, 2473-2479, 10.1016/j.atmosenv.2011.02.045, 2011.

919 Wang, J., Onasch, T. B., Ge, X., Collier, S., Zhang, Q., Sun, Y., Yu, H., Chen, M., Prévôt, A. S.  
920 H., and Worsnop, D. R.: Observation of Fullerene Soot in Eastern China, *Environ. Sci.*  
921 *Technol. Lett.*, 3, 121-126, 10.1021/acs.estlett.6b00044, 2016a.

922 Wang, Q., Sun, Y., Jiang, Q., Du, W., Sun, C., Fu, P., and Wang, Z.: Chemical composition of  
923 aerosol particles and light extinction apportionment before and during the heating season in  
924 Beijing, China, *J. Geophys. Res. - Atmos.*, 120, 2015JD023871, 10.1002/2015JD023871,  
925 2015.

926 Wang, Q., Zhao, J., Du, W., Ana, G., Wang, Z., Sun, L., Wang, Y., Zhang, F., Li, Z., Ye, X.,  
927 and Sun, Y.: Characterization of submicron aerosols at a suburban site in central China, *Atmos*  
928 *Environ.*, 131, 115-123, <http://dx.doi.org/10.1016/j.atmosenv.2016.01.054>, 2016b.

929 Wexler, A. S., and Johnston, M. V.: What have we learned from highly time-resolved

930 measurements during EPA's Supersites program, and related studies?, *J. Air Waste Manage.*,  
931 58, 303-319, 10.3155/1047-3289.58.2.303, 2008.

932 Xu, J., Zhang, Q., Chen, M., Ge, X., Ren, J., and Qin, D.: Chemical composition, sources, and  
933 processes of urban aerosols during summertime in northwest China: insights from  
934 high-resolution aerosol mass spectrometry, *Atmos. Chem. Phys.*, 14, 12593-12611,  
935 10.5194/acp-14-12593-2014, 2014.

936 Xu, W. Q., Sun, Y. L., Chen, C., Du, W., Han, T. T., Wang, Q. Q., Fu, P. Q., Wang, Z. F., Zhao,  
937 X. J., Zhou, L. B., Ji, D. S., Wang, P. C., and Worsnop, D. R.: Aerosol composition, oxidation  
938 properties, and sources in Beijing: results from the 2014 Asia-Pacific Economic Cooperation  
939 summit study, *Atmos. Chem. Phys.*, 15, 13681-13698, 10.5194/acp-15-13681-2015, 2015.

940 Yan, J., Chen, L., Lin, Q., Li, Z., Chen, H., and Zhao, S.: Chemical characteristics of  
941 submicron aerosol particles during a long-lasting haze episode in Xiamen, China, *Atmos.*  
942 *Environ.*, 113, 118-126, 10.1016/j.atmosenv.2015.05.003, 2015.

943 Yang, H., Yu, J. Z., Ho, S. S. H., Xu, J. H., Wu, W. S., Wan, C. H., Wang, X. D., Wang, X. R.,  
944 and Wang, L. S.: The chemical composition of inorganic and carbonaceous materials in PM<sub>2.5</sub>  
945 in Nanjing, China, *Atmos. Environ.*, 39, 3735-3749, 10.1016/j.atmosenv.2005.03.010, 2005.

946 Yang, L.-X., Wang, D.-c., Cheng, S.-h., Wang, Z., Zhou, Y., Zhou, X.-h., and Wang, W.-x.:  
947 Influence of meteorological conditions and particulate matter on visual range impairment in  
948 Jinan, China, *Sci. Total Environ.*, 383, 164-173, 10.1016/j.scitotenv.2007.04.042, 2007.

949 Yeung, M. C., Lee, B. P., Li, Y. J., and Chan, C. K.: Simultaneous HTDMA and  
950 HR-ToF-AMS measurements at the HKUST Supersite in Hong Kong in 2011, *J. Geophys.*  
951 *Res. - Atmos.*, 2013JD021146, 10.1002/2013JD021146, 2014.

952 Young, D. E., Kim, H., Parworth, C., Zhou, S., Zhang, X., Cappa, C. D., Seco, R., Kim, S.,  
953 and Zhang, Q.: Influences of emission sources and meteorology on aerosol chemistry in a  
954 polluted urban environment: results from DISCOVER-AQ California, *Atmos. Chem. Phys.*,  
955 16, 5427-5451, 10.5194/acp-16-5427-2016, 2016.

956 Yu, L., Smith, J., Laskin, A., Anastasio, C., Laskin, J., and Zhang, Q.: Chemical  
957 characterization of SOA formed from aqueous-phase reactions of phenols with the triplet  
958 excited state of carbonyl and hydroxyl radical, *Atmos. Chem. Phys.*, 14, 13801-13816,  
959 10.5194/acp-14-13801-2014, 2014.

960 Zhang, J. K., Sun, Y., Liu, Z. R., Ji, D. S., Hu, B., Liu, Q., and Wang, Y. S.: Characterization  
961 of submicron aerosols during a month of serious pollution in Beijing, 2013, *Atmos. Chem.*  
962 *Phys.*, 14, 2887-2903, 10.5194/acp-14-2887-2014, 2014.

963 Zhang, J. K., Wang, L. L., Wang, Y. H., and Wang, Y. S.: Submicron aerosols during the  
964 Beijing Asia-Pacific Economic Cooperation conference in 2014, *Atmos. Environ.*, 124, Part  
965 B, 224-231, 10.1016/j.scitotenv.2007.04.042, 2016a.

966 Zhang, Q., Alfarra, M. R., Worsnop, D. R., Allan, J. D., Coe, H., Canagaratna, M. R., and  
967 Jimenez, J. L.: Deconvolution and quantification of hydrocarbon-like and oxygenated organic  
968 aerosols based on aerosol mass spectrometry, *Environ. Sci. Technol.*, 39, 4938-4952,  
969 10.1021/Es0485681, 2005.

970 Zhang, Q., Jimenez, J. L., Canagaratna, M. R., Allan, J. D., Coe, H., Ulbrich, I., Alfarra, M. R.,  
971 Takami, A., Middlebrook, A. M., Sun, Y. L., Dzepina, K., Dunlea, E., Docherty, K., DeCarlo,  
972 P. F., Salcedo, D., Onasch, T., Jayne, J. T., Miyoshi, T., Shimono, A., Hatakeyama, S.,  
973 Takegawa, N., Kondo, Y., Schneider, J., Drewnick, F., Borrmann, S., Weimer, S., Demerjian,  
974 K., Williams, P., Bower, K., Bahreini, R., Cottrell, L., Griffin, R. J., Rautiainen, J., Sun, J. Y.,  
975 Zhang, Y. M., and Worsnop, D. R.: Ubiquity and dominance of oxygenated species in organic  
976 aerosols in anthropogenically-influenced Northern Hemisphere midlatitudes, *Geophys. Res.*  
977 *Let.*, 34, L13801, 10.1029/2007gl029979, 2007a.

978 Zhang, Q., Jimenez, J. L., Worsnop, D. R., and Canagaratna, M.: A case study of urban  
979 particle acidity and its influence on secondary organic aerosol, *Environ. Sci. Technol.*, 41,  
980 3213-3219, 10.1021/Es061812j, 2007b.

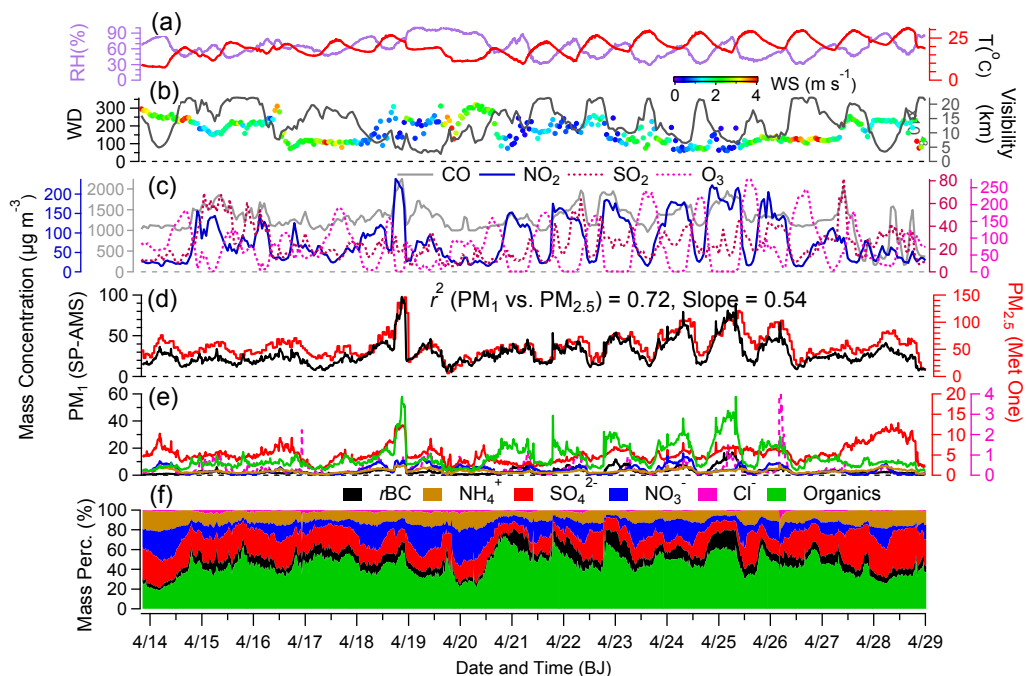
981 Zhang, Q., Jimenez, J., Canagaratna, M., Ulbrich, I., Ng, N., Worsnop, D., and Sun, Y.:  
982 Understanding atmospheric organic aerosols via factor analysis of aerosol mass spectrometry:  
983 a review, *Anal. Bioanal. Chem.*, 401, 3045-3067, 10.1007/s00216-011-5355-y, 2011.

984 Zhang, Y. J., Tang, L. L., Wang, Z., Yu, H. X., Sun, Y. L., Liu, D., Qin, W., Canonaco, F.,  
985 Prévôt, A. S. H., Zhang, H. L., and Zhou, H. C.: Insights into characteristics, sources, and  
986 evolution of submicron aerosols during harvest seasons in the Yangtze River delta region,  
987 China, *Atmos. Chem. Phys.*, 15, 1331-1349, 10.5194/acp-15-1331-2015, 2015.

988 Zhang, Y. J., Tang, L., Yu, H., Wang, Z., Sun, Y., Qin, W., Chen, W., Chen, C., Ding, A., Wu,  
989 J., Ge, S., Chen, C., and Zhou, H.-c.: Chemical composition, sources and evolution processes  
990 of aerosol at an urban site in Yangtze River Delta, China during wintertime, *Atmos. Environ.*,  
991 123, 339-349, 10.1016/j.atmosenv.2015.08.017, 2016b.

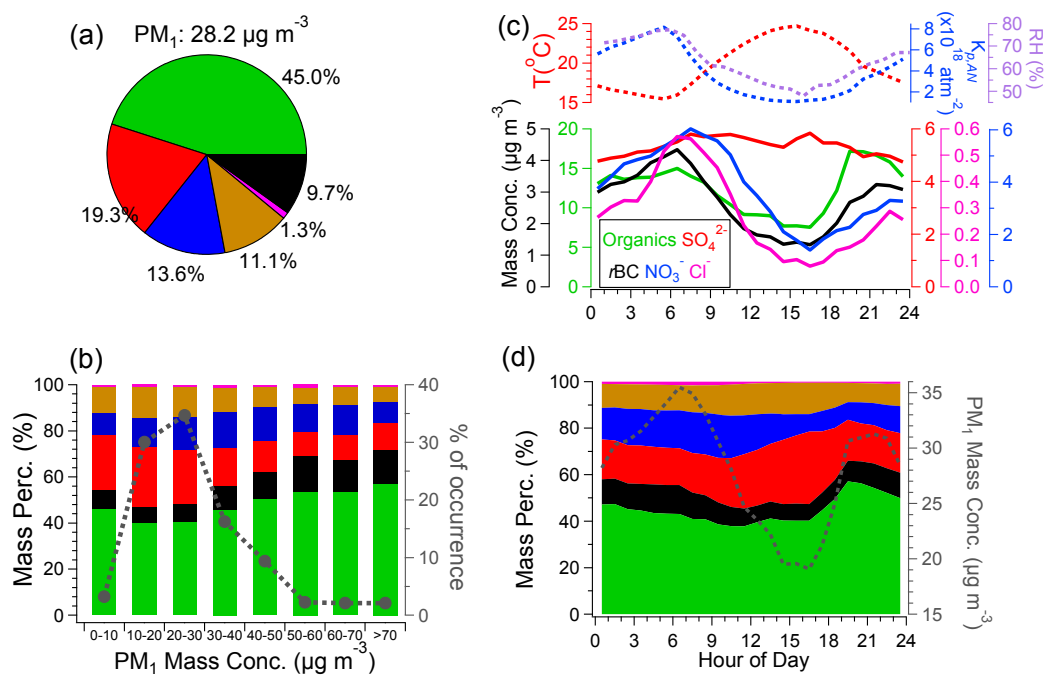
992  
993  
994





995  
 996 Figure 1. Time series of (a) relative humidity (RH) and temperature (T), (b) wind  
 997 direction (WD) colored by wind speed (WS,  $\text{m s}^{-1}$ ) and visibility (km), (c) mass  
 998 concentrations of CO, NO<sub>2</sub>, SO<sub>2</sub> and O<sub>3</sub> (hourly data), (d) mass concentrations of PM<sub>1</sub>  
 999 measured by the SP-AMS, and PM<sub>2.5</sub> measured by the co-located Met One PM<sub>2.5</sub>  
 1000 analyzer, (e) mass concentrations of rBC, ammonium, sulfate, nitrate, chloride and  
 1001 organics, and (f) mass contributions (%) of the six PM<sub>1</sub> components (BJ, Beijing).  
 1002

1003



1004

1005

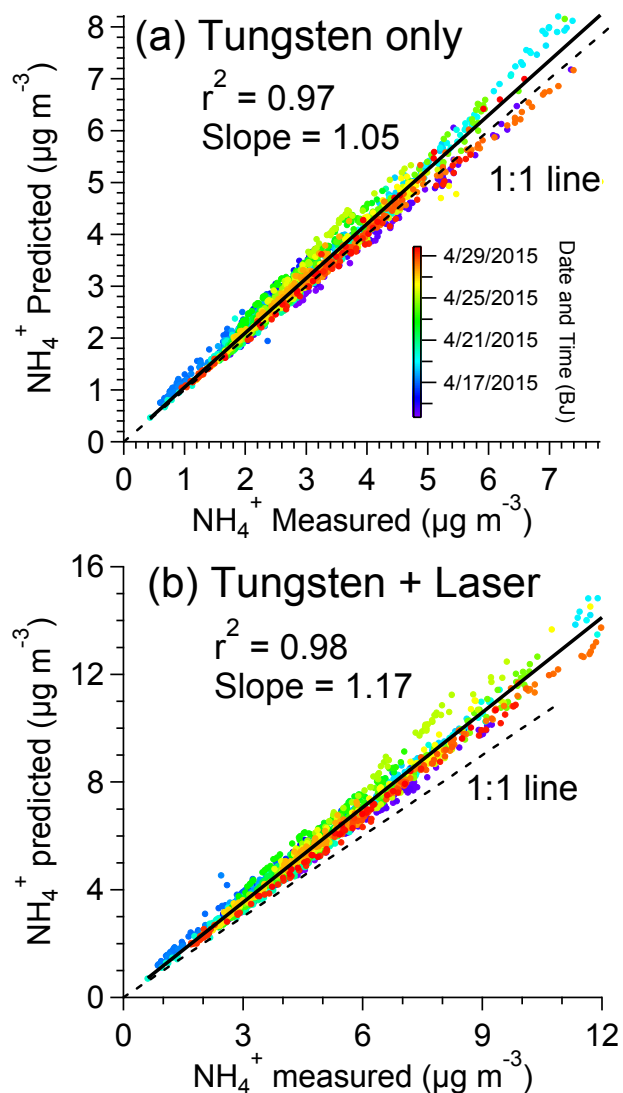
1006 Figure 2. (a) Campaign-averaged mass contributions of organics, sulfate, nitrate,  
 1007 ammonium, chloride and  $rBC$  to the total  $PM_{10}$ , (b) mass percentages of the six  $PM_{10}$   
 1008 species (left y-axis) and, fractions of the number of data points to the total number of  
 1009 data points for  $PM_{10}$  at different concentration bins (right y-axis), (c) diurnal patterns  
 1010 of mass concentrations of the major  $PM_{10}$  species (bottom panel), temperature (top  
 1011 panel, left y-axis), relative humidity (RH) (top panel, right y-axis), and the equilibrium  
 1012 constant ( $K_{p,AN}$ ) of  $NH_4NO_3$  (top panel, right y-axis)

1013 ( $K_{p,AN} = K_{p,AN}(298)exp\left\{a\left(\frac{298}{T} - 1\right) + b\left[1 + \ln\left(\frac{298}{T}\right) - \frac{298}{T}\right]\right\}$ , for reaction

1014  $NH_4NO_3(p) \leftrightarrow NH_3(g) + HNO_3(g)$ .  $K_{p,AN}(298)$  is the equilibrium constant at 298 K  
 1015 ( $3.36 \times 10^{16} atm^{-2}$ ),  $a = 75.11$ , and  $b = -13.5$  (Seinfeld and Pandis, 2006)), (d) diurnal  
 1016 variations of mass fractional contributions of the six  $PM_{10}$  species (left y-axis), and the  
 1017  $PM_{10}$  mass concentrations (right y-axis).

1018

1019



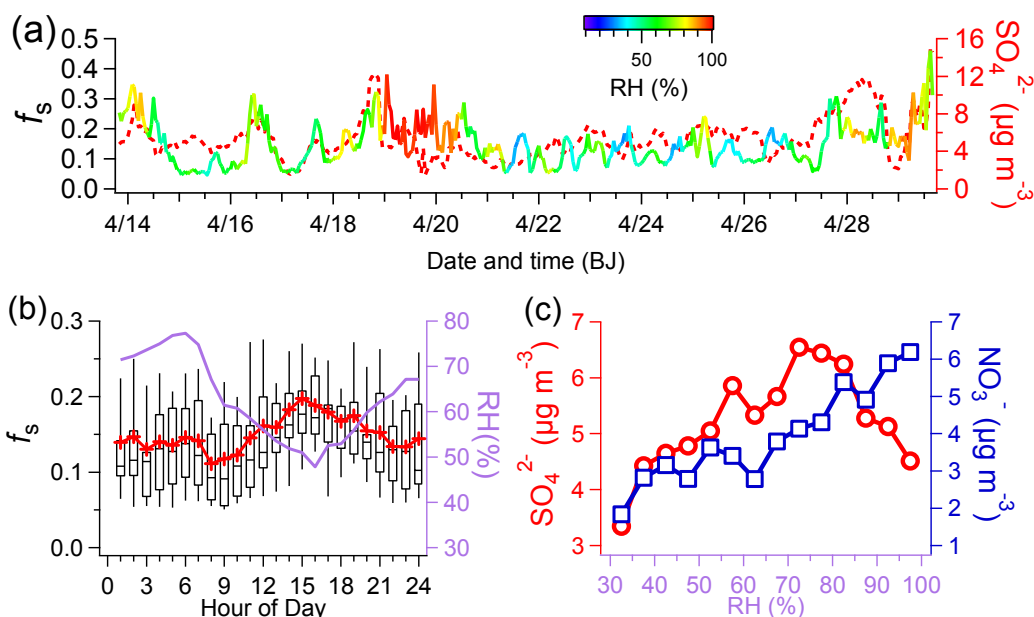
1020

1021 Figure 3. Scatter plots of the predicted  $\text{NH}_4^+$  vs. measured  $\text{NH}_4^+$  concentrations  
 1022 (colored by time), in the case of (a) tungsten vaporizer only, and (b) dual-vaporizers  
 1023 (tungsten + laser). The predicted values were calculated according to the formula:  
 1024  $\text{NH}_4^+$  predicted =  $18 \times (2 \times \text{SO}_4^{2-} / 96 + \text{NO}_3^- / 62 + \text{Cl}^- / 35.5)$  (Zhang et al., 2007b).

1025

1026

1027



1028

1029

1030

1031

1032

1033

1034

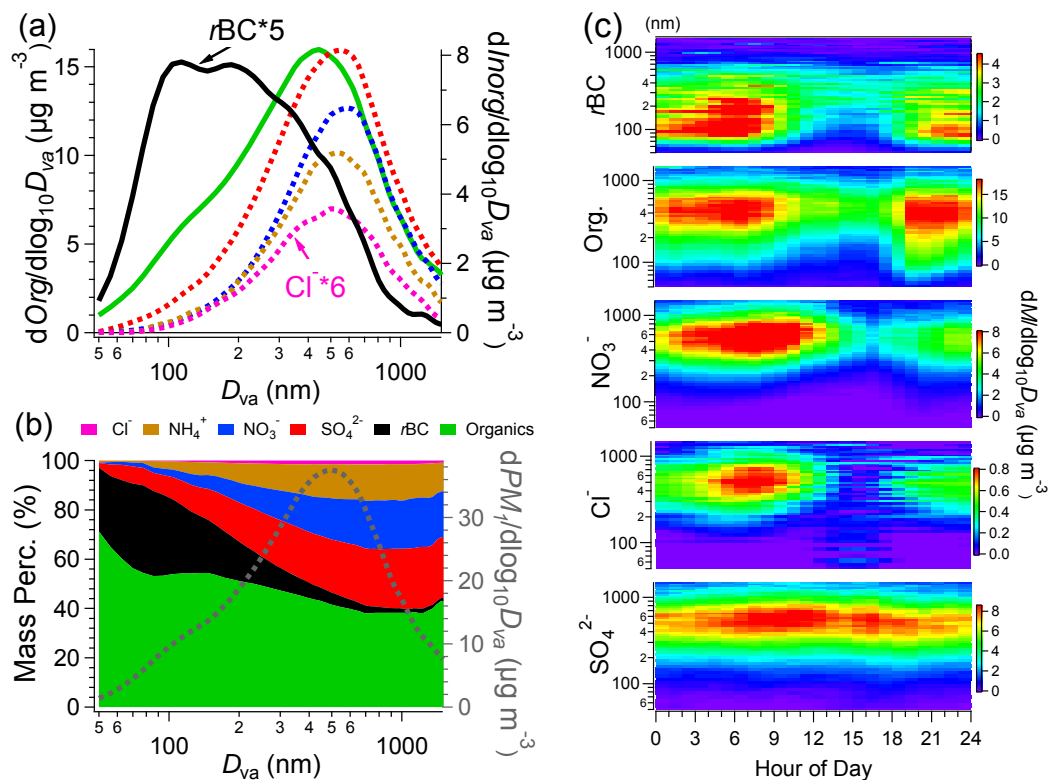
1035

1036

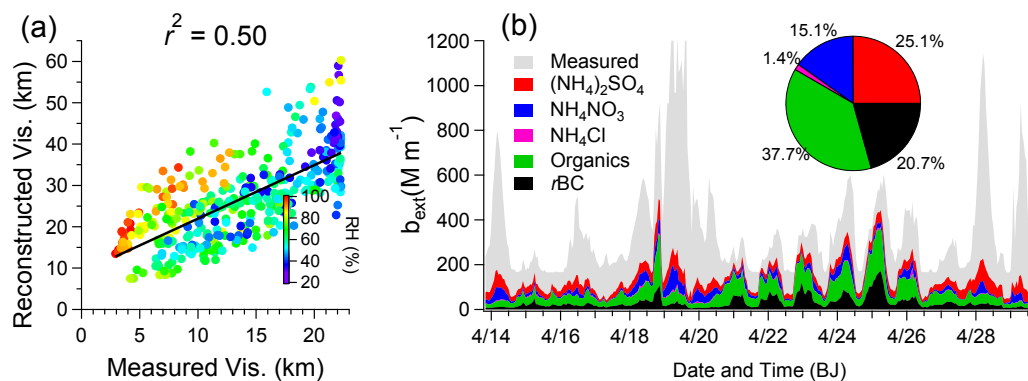
1037

1038

Figure 4. Time series of (a) sulfur oxidation ratio,  $f_s = nSO_4^{2-}/(nSO_4^{2-} + nSO_2)$ , and sulfate, (b) diurnal variations of  $f_s$  and RH (the lines and cross symbols indicate the mean values, the lines in the boxes indicate the median values, the upper and lower boundaries of the boxes indicate the 75th and 25th percentiles, and the whiskers above and below the boxes indicate the 90th and 10th percentiles), (c) Sulfate and nitrate concentrations vs. RH, the circles or squares represent the average concentrations within different RH bins (5% increment) for sulfate and nitrate, respectively.



1039  
 1040 Figure 5. (a) Mass-based average size distributions of organics,  $rBC$  (left y-axis),  
 1041 sulfate, nitrate, chloride and ammonium (right y-axis) ( $D_{va}$ , vacuum aerodynamic  
 1042 diameter), (b) fractional contributions of the six  $PM_{10}$  species as a function of particle  
 1043 size (left y-axis), and size distribution of total  $PM_{10}$  (right y-axis), (c) diurnal profiles  
 1044 of the size distributions of  $rBC$ , organics, nitrate, chloride and sulfate.  
 1045  
 1046



1047

1048

1049

1050

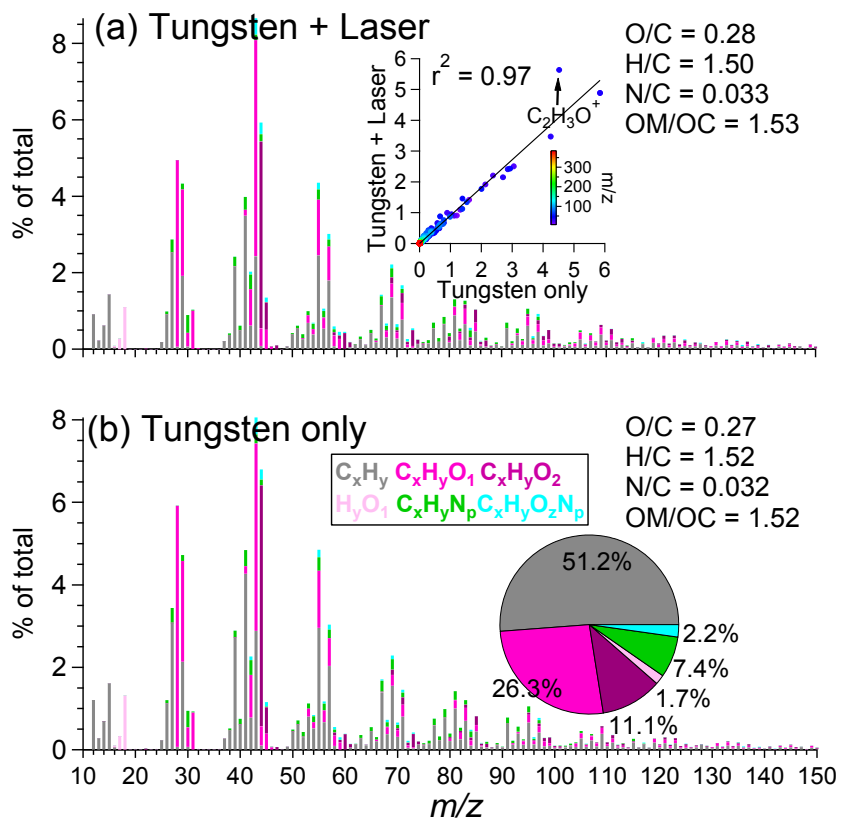
1051

1052

1053

1054

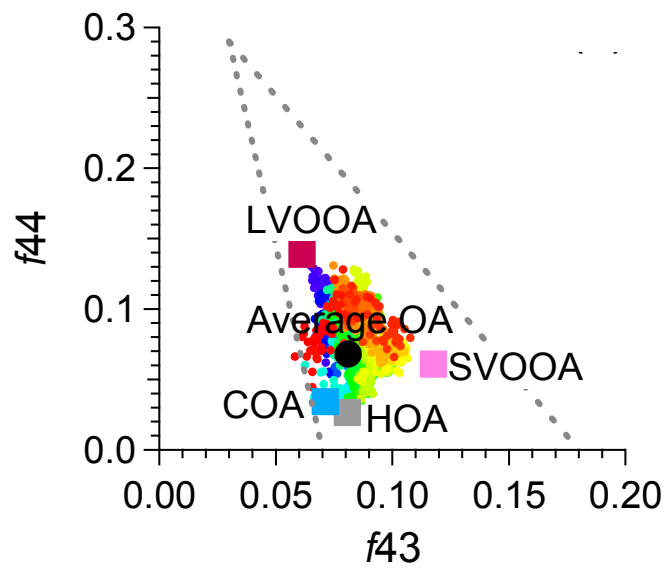
Figure 6. (a) Scatter plot of reconstructed vs. measured visibility (colored by RH), (b) light extinction coefficients derived from measured visibility (grey), and reconstructed from SP-AMS measured ammonium sulfate, ammonium nitrate, ammonium chloride, organics and  $rBC$  using the IMPROVE method. The inset pie shows the relative contributions of the five species to the light extinction of  $PM_{10}$ .



1055

1056 Figure 7. Campaign-averaged high resolution mass spectra of OA colored by six ion  
 1057 categories, in the case of (a) dual-vaporizers (tungsten + laser) (the inset scatter plot  
 1058 compares the spectral similarity between (a) and (b)), and (b) tungsten vaporizer only  
 1059 (the inset pie shows the relative contributions of six ion categories to the total OA).

1060



1061

1062 Figure 8. Triangle plot of  $f_{44}$  vs.  $f_{43}$  for all OA (colored by time), and the four OA  
 1063 factors identified by the PMF analyses.

1064

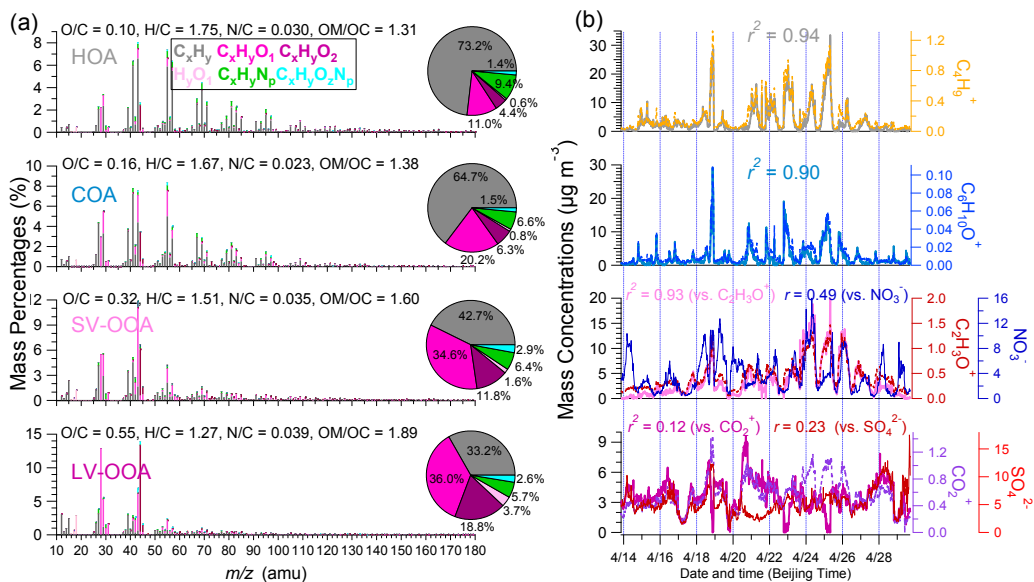
1065

1066

1067

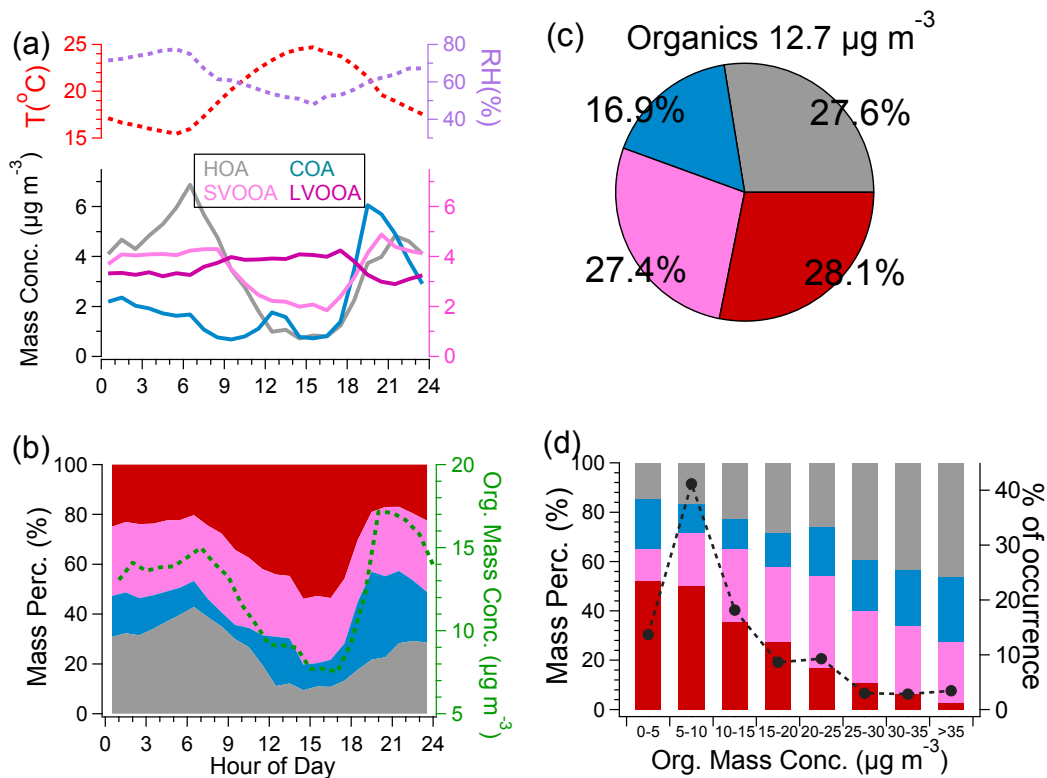
1068





1069  
 1070  
 1071  
 1072  
 1073  
 1074  
 1075  
 1076  
 1077

Figure 9. (a) High resolution mass spectra of hydrocarbon-like OA (HOA), cooking-related OA (COA), semi-volatile oxygenated OA (SV-OOA), and low volatility oxygenated OA (LV-OOA) colored by six ion categories (the four inset pies show the relative contributions of the six ion categories to the four OA factors, respectively), (b) time series of the four OA factors, corresponding tracer ions, nitrate and sulfate.



1078

1079

1080

1081

1082

1083

1084

1085

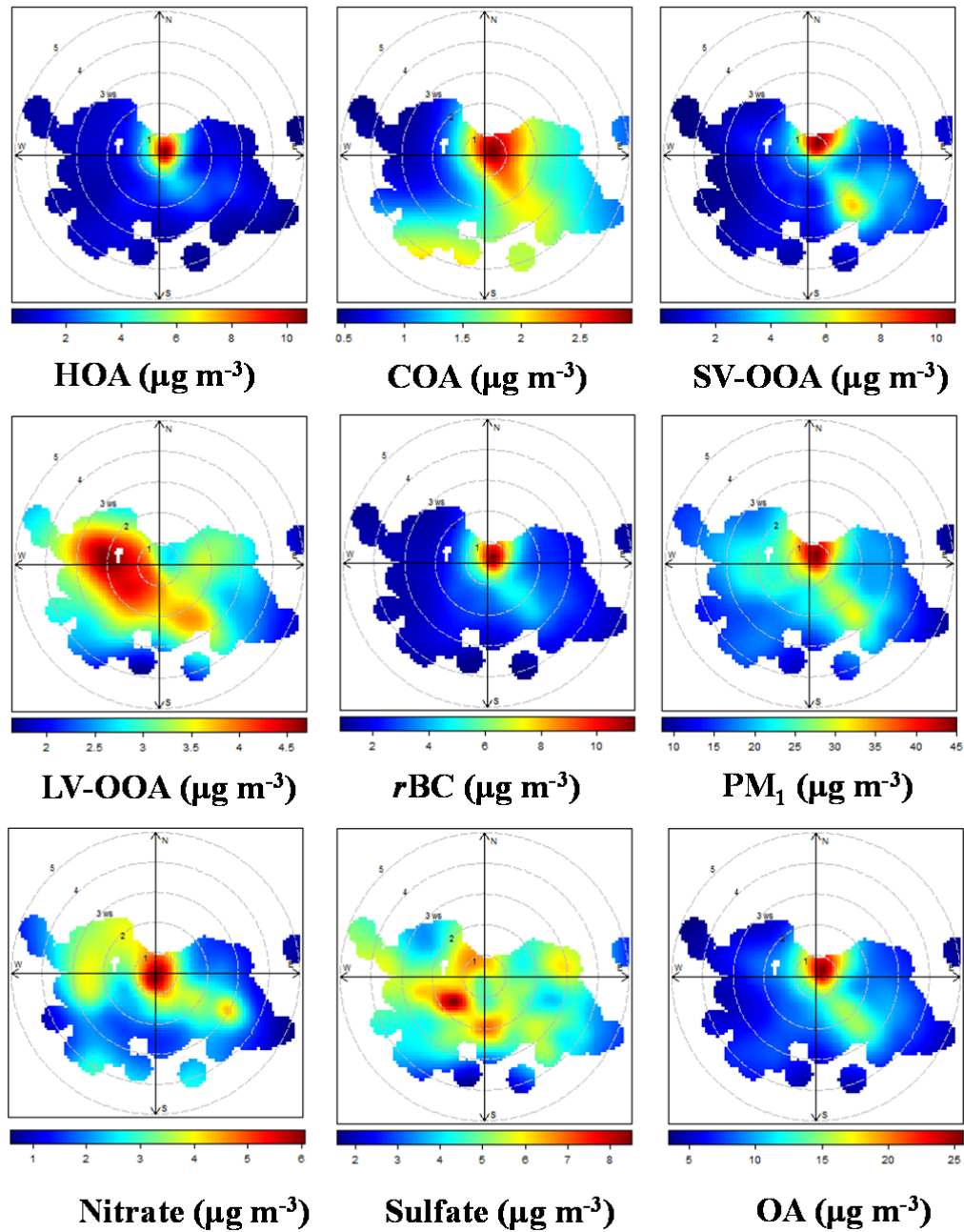
1086

1087

1088

1089

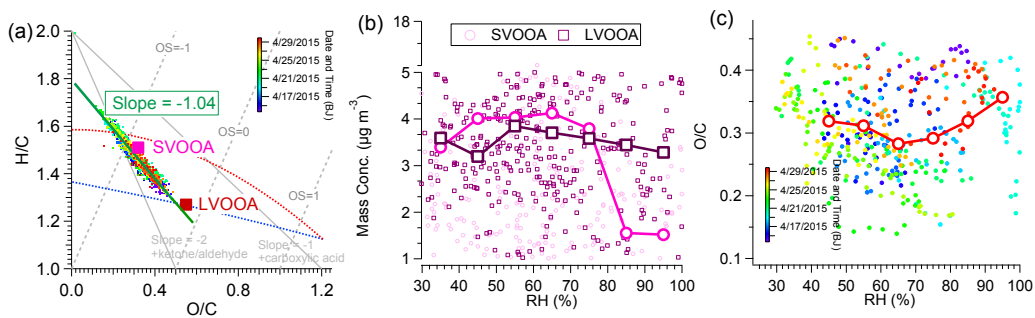
Figure 10. (a) Diurnal cycles of mass concentrations of the four OA factors (bottom panel), temperature (top panel, left y-axis) and RH (top panel, right y-axis), (b) diurnal variations of mass contributions of the four OA factors (left y-axis), and the total OA mass concentrations (right y-axis), (c) campaign-averaged mass contributions of the four OA factors to the total OA mass, and (d) mass contributions of the four OA factors (left y-axis), and the fractions of the number of data points to the total number of data points for the OA at different concentration ranges (right y-axis).



1090  
1091  
1092  
1093  
1094  
1095

Figure 11. Bivariate polar plots of HOA, COA, SV-OOA, LV-OOA,  $r\text{BC}$ ,  $\text{PM}_{1}$ , nitrate, sulfate and the total OA (the color scale shows the concentration of each species, and the radial scale shows the wind speed that increases outward from the center).

1096  
1097



1098  
1099  
1100  
1101  
1102  
1103  
1104  
1105  
1106  
1107  
1108

Figure 12. (a) Van Krevelen diagram of H/C vs. O/C ratios for all OA data colored by time, the blue and red dashed lines correspond to the right and left grey dashed lines in the  $f_{44}$  vs.  $f_{43}$  triangle plot of Fig. 8, the grey lines represents the addition of a particular functional group to an aliphatic carbon (Heald et al., 2010), (b) scatter plot of SVOOA and LVOOA mass concentrations vs. RH, the circles or squares represent the average mass concentrations within different RH bins (10% increment) for SVOOA and LVOOA, respectively, (c) scatter plot of O/C vs. RH (colored by time), the circles represent the average O/C values within different RH bins (10% increment).

1109 Table 1. Correlation coefficients (Pearson's  $r^2$ ) between the mass spectral profiles of  
 1110 the OA factors identified in this work with the corresponding factors identified in  
 1111 Beijing (2013 Winter) (Sun et al., 2015a), Lanzhou (2014 Summer) ((Xu et al., 2014)),  
 1112 and Fresno (2010 Winter) (Ge et al., 2012b).  
 1113

Nanjing (2015 Spring)	High resolution MS ( $r^2$ )		
	Beijing (2013 Winter)	Lanzhou (2012 Summer)	Fresno (2010 Winter)*
HOA	0.92	0.90	0.98
COA	0.93	0.94	0.93
SV-OOA	0.68	0.75	0.90
LV-OOA	0.91	0.98	0.87
Unit mass resolution MS ( $r^2$ )			
HOA	0.92	0.91	0.99
COA	0.96	0.96	0.95
SV-OOA	0.70	0.74	0.91
LV-OOA	0.90	0.98	0.89

1114 \*Note the Fresno (2010 Winter) study only identified one OOA factor, we thus  
 1115 compared both SV-OOA and LV-OOA in this study with it.

1116 Table 2. Correlation coefficients (Pearson's  $r$ ) between the time series of the four OA  
 1117 factors with the gas-phase species (hourly data) and other PM<sub>1</sub> components (15-min  
 1118 data), and the correlation coefficients between the diurnal data.  
 1119

Pearson's $r$	Temp.(T)	Hourly data				15-min data			
		CO	NO <sub>2</sub>	SO <sub>2</sub>	O <sub>3</sub>	SO <sub>4</sub> <sup>2-</sup>	NO <sub>3</sub> <sup>-</sup>	Cl <sup>-</sup>	$r_{BC}$
HOA	-0.14	<u>0.71</u>	<u>0.77</u>	0.13	-0.54	0.15	0.26	0.45	0.92
COA	0.11	0.50	0.58	-0.06	-0.22	0.19	0.07	0.08	0.61
SVOOA	0.19	0.41	0.70	0.14	-0.21	<u>0.11</u>	<u>0.49</u>	0.25	0.70
LVOOA	0.069	-0.2	-0.18	0.06	0.14	<u>0.23</u>	<u>0.11</u>	0.01	-0.22
Diurnal data									
HOA	-0.94	0.86	0.86	0.66	-0.96	-0.35	0.72	0.82	<u>0.99</u>
COA	-0.15	0.28	0.59	-0.24	-0.24	-0.57	-0.33	-0.25	0.19
SVOOA	<u>-0.85</u>	0.86	0.94	0.58	-0.90	-0.51	0.53	0.61	0.89
LVOOA	<u>0.76</u>	-0.58	-0.83	-0.27	0.77	<u>0.72</u>	-0.26	-0.33	-0.75

1120

1121